Experimental and Theoretical Study on Enhancing Effect of Capillary Evaporation

相馬　秀

Acknowledgments

First of all, I would like to express my deepest gratitude to Professor Kunugi Tomoaki and Professor Yokomine Takehiko. Professor Kunugi has offered me an opportunity to obtain important knowledge on the topic of phase change and interface phenomena with his kind guidance and enthusiastic encouragement of this research. I am extremely grateful that he has taught me the ABCs of scientific research. Professor Yokomine has kindly accepted me as his doctoral student, despite guidance from the middle. This research would not be accomplished without his kind guidance and practical supports. He has also given me a chance to know the importance of having an engineering perspective, which I believe will be helpful for my future work.

I would also like to extend my sincere thanks to other members of my thesis committee: Professor Sasaki and Professor Suzuki for generously offering their time and suggestions. I must also very much thank Dr. Kawara for his supports and valuable comments on my research. Especially, his in-depth knowledge and helpful advice to experimental methods have contributed to this research.

Many thanks also to Dr. Yonemoto at Kumamoto University and Dr. Ueki at Osaka University for their supports. I am very grateful that they encouraged me every time we met at conferences.

Special thanks to Ms. Soejima for her practical help in this research. She has always been kind and my research-life has become much easier and more enjoyable. I also had the pleasure of working with Mr. Takeyama, Ms. Wang, Mr. Ando, Mr. Go, Mr. Teramoto, Mr. Huang and other lab members.

Lastly, I would like to thank my parents and my sister for their love and supports in many years. Without them, this day would not have been possible.

Kyoto University, March 2020
Soma Shu

Table of contents

Nomenclatures

A	area (m^2)
A_d	dispersion constant divided by -6π (J)
a, b	fitting parameter in Eq. (2.1)
a_m	molecular length (m)
c	vapor concentration (kg m^{-3})
c_1, c_2	coefficients in Eq. (5.15)
c_3, c_4	coefficients in Eq. (5.17)
c_5	coefficient in Eq. (5.18)
D	diffusion coefficient (m^2 s^{-1})
D_1, D_2	dimensionless quantities in Table 5-1
d	channel size (m)
F	free energy density (J m^{-1})
F_0	homogeneous part of free energy density (J m^{-1})
f	dimensionless evaporation coefficient
G	potential energy due to gravitational force (J m^{-2})
g	gravitational acceleration (m s^{-2})
H	Schrage's accommodation coefficient
h	distance from pool to contact line (m)
h_{fg}	enthalpy of vaporization (J kg^{-1})
J	normalized local evaporation flux
$\hat{J}$	normalized local evaporation flux in Eq.(5.27)
j	local evaporation flux (kg $m^{-2}s^{-1}$)
k	mass transfer coefficient (m s^{-1})
ℓ	diffusion length scale (m)
$\dot{m}$	evaporation rate (kg s^{-1})
n	refractive index
P	normalized pressure

$P(u)$	potential energy due to intermolecular forces (Jm^{-2})
p	pressure (Pa)
p_{in}	perimeter (m)
p'	pressure scale (Pa)
R	dimensionless reciprocal overall resistance
R_1, R_2	dimensionless quantities in Table 5-1
R_v	specific gas constant ($J\ kg^{-1}K^{-1}$)
Re_m	Reynolds number
$\mathbf{r} = (r, \varphi_i, z_i)$	cylindrical coordinate (see Fig. 4-1)
$\mathbf{r} = (r, \phi_i, \varphi_i)$	spherical coordinate (see Fig. 4-1)
S	dimensionless shape factor
T^*	temperature (K)
T	normalized temperature
t	time period (s)
ΔT^*	temperature scale (K)
U	normalized film thickness
u	liquid film thickness (m)
V	volume of gas phase (m^3)
v'	liquid velocity scale ($m\ s^{-1}$)
w	channel width (m)
X	normalized x coordinate
X_1, X_2	dimensionless quantities in Table 5-1
x	x-coordinate (m)
y	y-coordinate (m)
α	dimensionless modification factor
β	dimensionless free parameter
δ	film thickness (m)
ε	pressure ratio
ϕ	camera angle (rad)

Θ	microscopic contact angle (rad)
θ	apparent contact angle (rad)
θ_ℓ	refraction angle (rad)
κ	curvature (m^{-1})
κ_{cap}^{-1}	capillary length (m)
λ_w	wavelength (m)
λ	thermal conductivity of liquid ($W\ m^{-1}K^{-1}$)
υ	kinetic viscosity of liquid ($m^2\ s^{-1}$)
Π	disjoining pressure (Pa)
ρ	density ($kg\ m^{-3}$)
σ	surface tension ($N\ m^{-1}$)

Subscripts

e	adsorbed film in equilibrium
cross	crosssection
i	interface
d	disjoining
eq	equilibrim
ex	excess
ℓ	liquid
sat	saturation
$sat, T = [T]_3$	saturation at temperature $[T]_3$
$sat, T = 1$	saturation at temperature $T = 1$
v	vapor phase
w	wall
o	center of curvature
ow	outer wall
0 ~ 3	physical quantities at boundary BC-0 ~ BC-3 (see Fig.5-1)
∞	far-field

Overline

$\bar{-}$	area-average

Brackets

$[\ ]_{0\sim3}$	physical quantities at boundary BC-0 ~ BC-3 (see Fig.5-1)

List of figures

List of tables

Chapter 1 Introduction

1.1 Background

Evaporation, the phase-change phenomenon from liquid to vapor, constantly takes place around us and is an underlying phenomenon of many engineering processes. For example, in nuclear power plants, nuclear energy is converted into and transported as the thermal energy via boiling coolant, which enables us to safely and stably provide a power supply. Heat and mass transfer associated with evaporation is of high interest in material science (inkjet-printing [1], fabrication of functional materials [2], etc.) and environmental engineering (membrane distillation [3], solar steam generator [4], etc.), too. Especially, evaporation at a 3-phase contact region is essentially important in these processes. The above-mentioned examples (inkjet, material fabrication, and so on) are based on wetting phenomenon, hence the characteristics of these processes are strongly affected by how liquid contacts with solid. Evaporation of wetting film is also of interest in the boiling process in terms of a contribution of wetting-film evaporation to bubble growth. Many research efforts have been performed to study the dynamics of boiling, which may advance thermal management in electronics.

To solve the engineering issue of predicting and controlling these processes in various situations, it is essential to enhance the physical knowledge of the underlying phenomenon. However, there exist open questions in the physics of evaporation at the wetting film. This will be clarified with reviewing previous important researches, in Section 1.3. Before that, in the next section, the basic features of the wetting film are reviewed with defining several terminologies used in this manuscript.

1.2 What is a wetting film?

The wetting film shows a liquid film covering a solid surface, partially or entirely. As an example, consider a solid plate is immersed in the liquid and kept stationary, as illustrated in Fig.1-1(a). Solid surface perturbs liquid surface and, if the wettability of the solid surface is high, the wedge-shaped liquid film called meniscus forms on the solid surface. The characteristic length of a meniscus is called capillary length defined as follows;

$$\kappa_{cap}^{-1} = \sqrt{\frac{\sigma}{\rho g}} \,. \tag{1.1}$$

σ, ρ, g are liquid surface tension, liquid density, and gravitational acceleration, respectively. The capillary length is derived by balancing capillary pressure and hydrostatic pressure. This length is important in wetting phenomena. If the length scale of interest is shorter than capillary length, the surface effect becomes significant over gravitational effect and arc-shaped meniscus forms (see inset of Fig.1-1(a)). In other words, the characteristic length of a meniscus is either capillary length κ_{cap}^{-1} or channel size d, whichever is smaller [5].

The shape of a wetting film is given as the condition where system free energy is minimized. One of the theoretical models is Young's relation [6]. This equation derived from the principle of minimum free energy is well-known as balances of each surface tension (gas-liquid, solid-liquid, solid-gas) projected onto the solid surface. The line where the 3-phases seem to contact each other is called an apparent contact line and the angle between the solid-liquid and liquid-vapor interfaces is called an apparent contact angle.

Although Young's relation is a well-defined model, the macroscopic theory is not always appropriate as the length scale becomes small, typically less than 1μm. It is because the effects of intermolecular forces become not negligible as the contact line is focused. The pioneering study on the effects of the intermolecular forces on wetting film has been conducted by Derjaguin [7]. Derjaguin found the relationship between the pressure applied to a liquid interlayer between quartz and its thickness in equilibrium. The introduced excess pressure in the thin liquid layer is called disjoining pressure. Conventionally, the wetting film is often divided into an adsorbed film region characterized by disjoining pressure, the macro region characterized by capillary pressure, and the transitional micro region, as illustrated in Fig. 1-1(b). There are some variations in how to call the sub-regions; an intrinsic meniscus and an evaporating thin film [8–10], or macro- and

micro-regions [11–13], for example. In this study, the latter case is used.

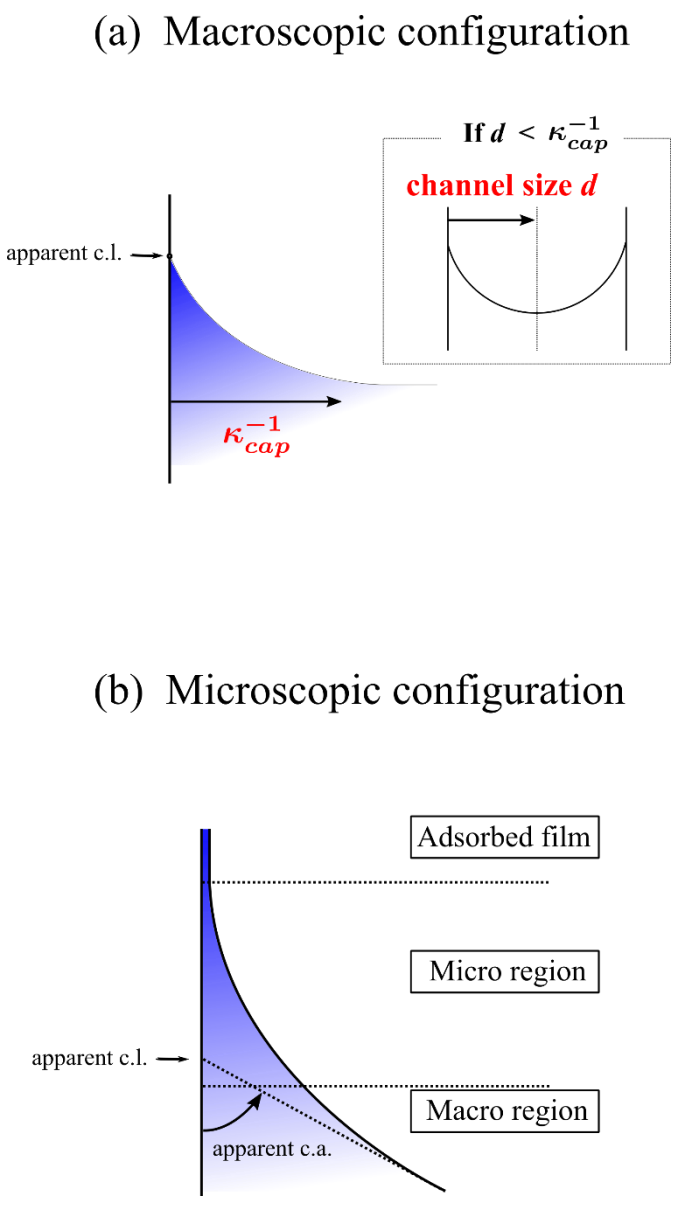

Fig. 1-1. (a) Meniscus whose characteristic length is capillary length κ_{cap}^{-1}. Inset: If channel size d is less than κ_{cap}^{-1}, the characteristic length of the meniscus is d. (b) Microscopic configuration of wetting liquid film near contact line (c.l.)

1.3 Studies on evaporation of wetting film

1.3.1 Theoretical studies

Potach & Wayner [14] conducted a pioneering study on the evaporation of wetting film. They built the model to describe the multiscale structure and local evaporation characteristics of a wetting film on a glass plate immersed in a carbon tetrachloride pool. In their model, the multiscale structure was described by mechanical balance considering disjoining pressure and capillary pressure. Heat and mass transfer is characterized by thermal resistance due to one-dimensional heat conduction of the liquid film and the interface resistance due to kinetic theory. Numerically solving the governing equations, they obtained the result that local evaporation flux is maximum in the micro region. This is due to the dependence of attractive intermolecular forces and the thermal resistance on liquid film thickness. In the adsorbed region, liquid molecules cannot escape to the gas phase because of attractive intermolecular forces. In other words, the adsorbed liquid film is thermodynamically equilibrium. The effect of attractive intermolecular forces rapidly weakens with increasing the film thickness and the film evaporates in the micro region. If evaporation is limited by the thermal resistance of the film, the local maximum of evaporation flux can be observed in the micro region as a result of a balance of intermolecular forces and the thermal resistance.

The menisci shapes predicted by their model showed the discontinuities due to an abrupt switch from one model to another at the transition region between the adsorbed and macro regions. Later, many researchers have proposed more sophisticated models to solve the problem. Moosman and Homsy [15] derived a nonlinear differential equation based on lubrication, thin liquid-film heat-transfer, and kinetic theory, and solved it as the lowest and next order problems of the perturbation series with wall superheat. In their models, equilibrium menisci shapes deform due to the stress field associated with flow caused by evaporation. In contrast to the models proposed by other studies [16–18], they clearly described an additional pressure term in the interface mechanical balance. This term acts as a source term in an expression of the evaporation flux. By using the Moosman and Homsy's expression, Morris [19] proposed a theory to predict the heat flow across the superheated wall by using ε, the pressure difference across the interface in the macro region normalized by the disjoining pressure at the contact line. He showed the linear and parabolic subregions in the micro region and used the perturbation expansion with $\varepsilon \to 0$. The nonlinear differential equation could be simplified by assuming a local equilibrium to give the higher-order differential equations for liquid film thickness [12,20]. There are so many other studies for pure

vapor conditions and the basic features of these thermal models can be summarized as follows;

- Assuming continuum fluid mechanics can be applied to wetting liquid film
- Evaporation flux characterized by the thermal resistance and interface resistance
- Local maxima of evaporation flux and interface curvature in the micro region

It must be noted that these models are only applicable to pure vapor conditions. For the open-air condition, several basic equations (e.g. Eqs. (2)-(7) in [21]) regarding thermodynamics and mechanical equilibrium do not hold. In this case, the thermodynamic approach [22] may be used to obtain the equilibrium shape of the wetting film.

1.3.2 Experimental studies

Evaporation on heated surface

DasGupta et al. have precisely measured shapes of menisci formed at the edge of the horizontal parallel plate [16–18,23] and at the cell corner [24] by using an ellipsometry and interference method. They analyzed local evaporation flux by fitting their model to the shape data and found different local interface curvature between the quasi-equilibrium case and wall heated case. In the quasi-equilibrium case, the interface curvature goes zero (adsorbed region) to a constant (macro region). Since the change in capillary pressure compensates with change in disjoining pressure, liquid pressure was found to be constant in this case. It was confirmed theoretically [25] and experimentally [26–29] that the interface curvature in the micro region is linear along with the solid surface. On the other hand, in the heated case, the interface curvature reached a local maximum in the micro region. This non-linearity of interface curvature is believed to lead pressure gradient driving liquid flow to the micro region where evaporation is significant due to the small thermal resistance.

The local maximum of evaporation flux on the heated wall accompanies evaporative cooling at the contact line, which was observed by Höhmann & Stephan [30]. They used a thermochromic liquid crystal to measure the heated wall temperature as meniscus evaporated between parallel plates. The schematic image of the temperature distribution they obtained is illustrated in Fig.1-2. The temperature was almost constant in the macro region while it sharply dropped near the

contact line. They thought the temperature changing region (~30μm in width) corresponds to the micro region because of the cooling effect. Dhavaleswarapu and coworkers measured temperature by an Infrared camera for heated solid surface under wetting IR-transparent heptane film [31,32]. Their energy-balance model showed about 70% [31] and 45% [32] of total heat transfer takes place from the micro region in their experimental system.

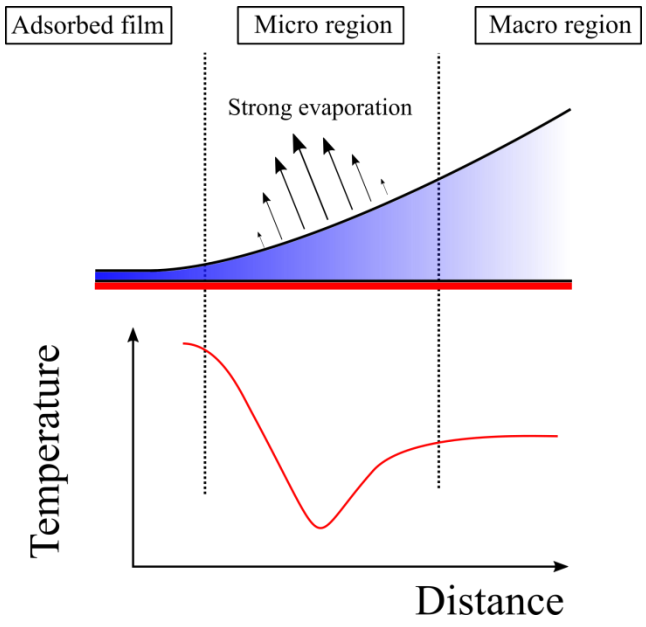

Fig. 1-2. Schematic picture of temperature distribution of heated surface underneath contact-line region (see Fig.6 in [30]).

The experimental studies mentioned above supports the thermal models mentioned in Section 1.3.1. On the other hand, there are some experimental results which cannot be explained by conventional models. Li and coworkers measured the water evaporation rates formed at the edge of nano-channel with various channel sizes [33]. The noteworthy and interesting finding was the evaporation rate per channel area (i.e. apparent evaporation flux) increased nonlinearly with reducing channel size. This result cannot be explained by the thermal models indicating significant evaporation in the micro region because the interface resistance due to the molecular kinetics in the Knudsen layer is much significant than the thermal resistance of the wetting film. They also found that the evaporation fluxes are several times larger than the maximum value predicted by the Hertz-Knudsen equation (the formula can be found [6] etc.). They postulated these tendencies is due to the increase in the meniscus area and analyzed their data with Narayanan's model [34]. The model describes elongation of the micro region due to the effect of intermolecular forces, mainly electric double layer forces, in the nanopore, which indeed shows the increase in apparent evaporation flux with reducing channel size. However, the model showed the unphysical result that the accommodation coefficient in the Hertz-Knudsen equation is more than 1. In their later experimental study on evaporation in nanopore [35], this tendency was explained by the precursor nanofilm [36]. In their new experiments, they fabricated a hydrophobic coat on the outer surface of nanopore to prevent the effective evaporation area from increasing. As a result, the evaporation flux became indeed smaller than the maximum value predicted by Hertz-Knudsen equation. On the other hand, it was still observed that the evaporation flux increased nonlinearly with reducing meniscus size. They suggested it is due to a dependence of accommodation coefficient on the electrochemical property of liquid, although the qualitative and quantitative validity of their suggestion is not clear.

Evaporation on non-heated surface

Buffone & Sefiane have published many experimental reports for thermocapillary Marangoni convection in volatile liquid meniscus formed at the edge of capillary tubes. Marangoni convection is the liquid flow driven by the surface tension gradient. Because surface tension is a function of interface temperature, the gradient of interface temperature induces the thermocapillary Marangoni convection. By the IR measurement for the interface temperature of evaporating meniscus, they confirmed that the center of the meniscus is warm while the contact-line region is cold [37,38] and the temperature gradient drives thermocapillary Marangoni

convection [39–41]. They suggested the temperature gradient could be due to the significant evaporation at the micro region, similar to the thermal models.

Furthermore, Buffone & Sefiane measured evaporation rates in capillary tubes with various tube sizes [42]. Fig.1-3 is their experimental configuration to show evaporating meniscus is pinned at the edge of capillary tubes while the rate of evaporation into atmosphere relates to the receding speed of another meniscus. They observed interesting results that evaporation rate linearly decreased and interface-area-averaged evaporation flux increased with reducing tube size. They claimed the linear increase in the evaporation rate is qualitatively consistent with their idea of significant evaporation in the micro region.

Their discussion shows evaporation rate and flux are determined by the tube radius [43]. However, despite solid is not heated, is such significant evaporation in the micro region really possible? They argued the temperature gradient from the meniscus center to the contact line region supports their idea, but is it correct? Another possibility is available; warm liquid is continuously supplied to meniscus base and evaporation at the macro region consumes the energy before supply to the pinned contact line. In other words, the contact line is relatively far from the supply of warm liquid. Indeed, in their later experiments where apparent contact angle was imposed by various rates of liquid supply, it was observed that the interface temperature distribution became flat for a flat interface, and even cold in the center for a convex meniscus [44]. This shows the interface temperature strongly depends on the liquid flow field. If the contribution of the micro region to the total evaporation rate is not significant, then, why smaller tube/channel size does exhibit stronger evaporation? As mentioned above, the increase in the effective evaporation area due to precursor nanofilm is another possible physics. However, the contribution of the precursor nanofilm may not be significant compared to the intrinsic surface of macro-liquids, according to the recent review [36].

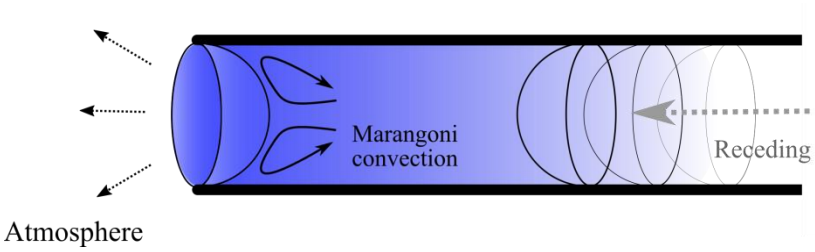

Fig. 1-3. Evaporation of organic liquid in capillary tube. Marangoni convection due to temperature gradient was observed in [42].

1.4 Objectives

As mentioned in the previous section, there are some open questions in the physics of evaporation of wetting film. One is whether the significant evaporation in the micro region is possible in the open air without artificially heating, as shown in Fig.1-4. If not, the enhancing effect of evaporation with reducing channel size must be re-considered. Because the experimental data in the presence of the vapor diffusion layer is not enough to discuss the first question, experiments would be necessary in this study. The important point is separating the two length scales; perimeter and curvature of a meniscus. The perimeter corresponding to contact-line length and the curvature corresponding to the characteristic length of meniscus were treated as the same parameter in the Buffone's experiments. Separating these lengths can be realized by using rectangle channels and by using the relation between the characteristic length of a meniscus, channel size, and capillary length (see Section 1.2). If the channel sizes are less than capillary length, rectangle-shaped channels enable to adjust the curvature of a meniscus with keeping the perimeter almost constant. On the other hand, channels whose size is more than capillary length enable to adjust the perimeter with keeping the meniscus curvature constant. In addition to the length separation, it is also necessary to analyze local evaporation characteristics by a model considering the film conduction, kinetics, and vapor diffusion. The model will be used to discuss the mechanism for the enhancing effect.

The flow chart in this study is illustrated in Fig. 1-5. First, the author researched the dependence of evaporation flux on geometrical configurations of channels by means of experiments with keeping perimeter constant and with keeping meniscus curvature constant. The circular capillary tubes were also used to compare the evaporation flux in the rectangle channels. The experimental data are used to examine the validity of the conventional theory and to make quantitatively clear the difference between the effects of perimeter and curvature on evaporation flux. The next step is to seek how to mathematically describe the experimentally-obtained dependence of the evaporation rate on the geometrical configuration as a general rule. The scaling law is derived by using a macroscopic model considering vapor diffusion transport. Lastly, the author proposes a conjecture for the evaporation enhancing effect in a narrow channel and introduced the missing term into a microscopic model considering the film conduction, kinetics, and vapor diffusion. The proposed model was applied to the experimental data and compared with the scaling law derived by the macroscopic model.

Chapter 2 and Chapter 3 describe the experimental works to investigate the dependence of

evaporation kinetics on channel geometries. Based on the experimental data, the effects of curvature and perimeter on evaporation flux are discussed in Chapter 2 and Chapter 3, respectively. These experiments include the measurements for the evaporation characteristics such as contact angles and temperatures. In Chapter 4, a macroscopic model is proposed to mathematically show the dependence of the evaporation rate on the interface curvature. The resulting equation is applied to the present and previous experimental data. In the last Chapter 5, a phenomenological microscopic model is proposed to reveal how the evaporation enhancing effect comes. Finally, the conclusions and possible applications are provided in Chapter 6.

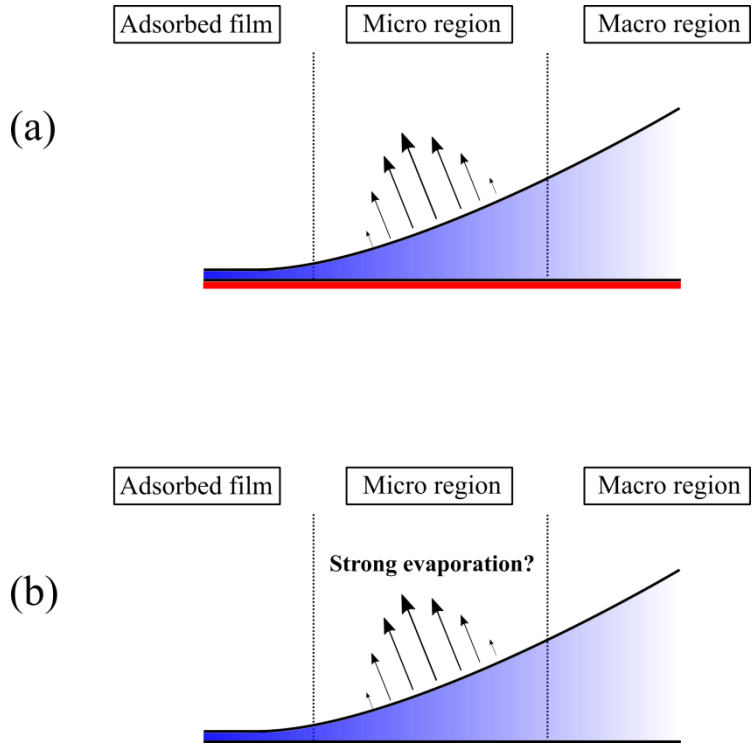

Fig. 1-4. Local evaporation characteristics in micro region on (a) heated solid surface and (b) non-heated solid surface

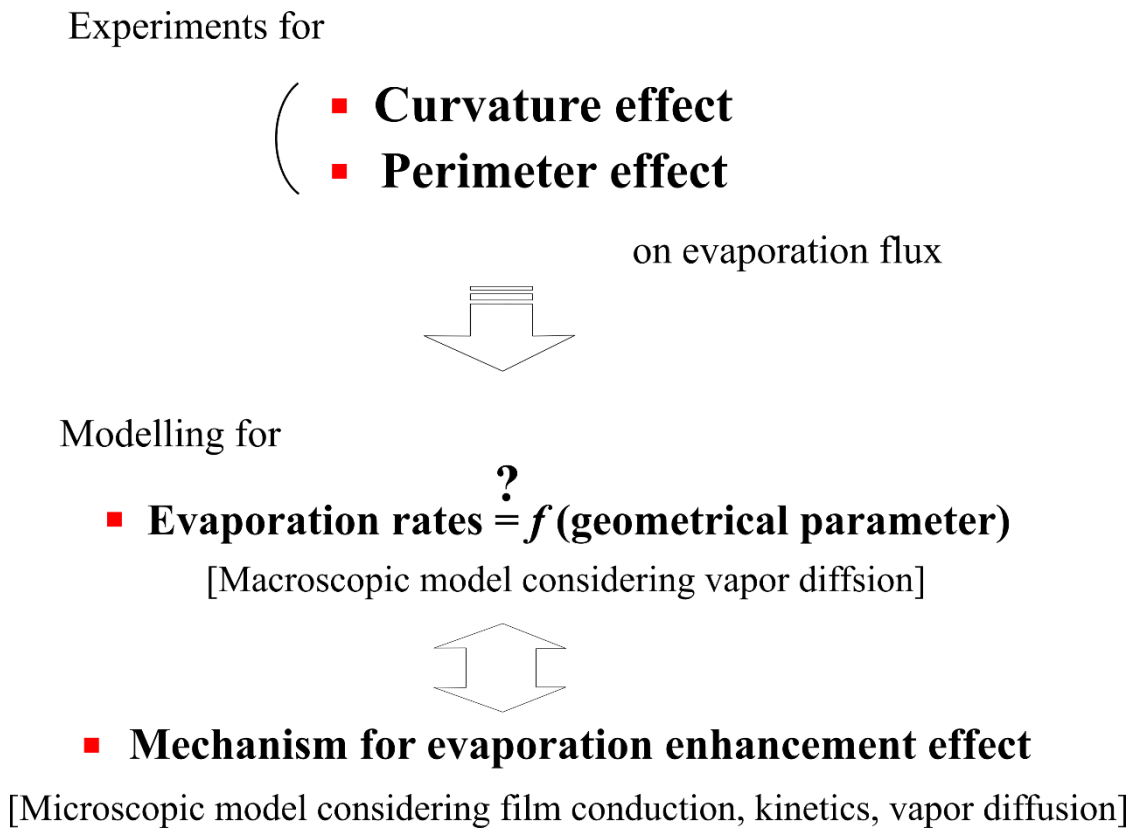

Fig. 1-5. Flow chart in this study

Chapter 2 Experiments for curvature effect

2.1 Introduction

This chapter discusses the experimental works for the effect of meniscus curvature on evaporation flux. In the previous experiments where capillary tubes were used [42], they could not distinguish the perimeter and curvature of meniscus because these changes were identical for capillary tubes. For this reason, the rectangle channel was used as a test section in the present experiments. The test channel used in Section 2.2.2 was designed for temperature measuring of the channel surfaces to quantify how much the diffusion-limited evaporation cools the surface. This chapter presents 2 different methods for measuring evaporation rates, indirect and direct methods.

2.2 Experimental apparatus and measuring techniques

2.2.1 Evaporation in glass channels

The evaporation rate, evaporation flux and contact angle of purified-water meniscus in a rectangle channel were experimentally obtained. As shown in Fig. 2-1(a), the test channel consists of two test plates and two Polystyrene endplates. The test plates are soda-lime glass (Muto Pure Chemicals co., ltd.) whose thickness is 1.0mm. To remove organic matters, surfaces of glass plates were wiped out by using ethanol (99.5 wt.%, Hayashi Pure Chemical Ind., Ltd.), rinsed by the purified water, and dried in atmosphere prior to the experiments. The clean surfaces of disposable Polystyrene endplates prepared by peeling off laminating films were used. The channel size d was set from 0.15mm to 0.75 mm by a thickness gauge sandwiched between the glass plates. The test channel consisting of the plates was stabilized in the cylindrical pool which was cleaned by ethanol and rinsed by purified water. Next, the working fluid was gently poured to the pool to form a meniscus at an equilibrium position between the plates due to the capillary force. As the working fluid, the author used the degassed purified water. After pouring working fluid, rapeseed oil was additionally poured on the pool surface to prevent water evaporation at the surface. The oil has low volatility as vapor pressures of the main components (Oleic acid and Linoleic acid) are ~0.1mPa [45] at room temperature and the vapor pressure of other components could also be negligible. The oil was kept from coming into the meniscus. It must be notable that the distance between the contact line to the channel exit was not measured in the present experiments, which could affect the evaporation rate because the diffusion resistance of vapor may be altered. In the next experiments in Section 2.2.2 and 3.2.2, the author will present the

experimental results obtained with a given distance between contact line to the channel exit.

The important point is the relation between the channel size d and capillary length κ_{cap}^{-1}. For water, the capillary length κ_{cap}^{-1} is 2.7mm. Because $d < \kappa_{cap}^{-1}$, the characteristic length of the meniscus is identical to d (see Fig.1-1). On the other hand, the change in the inner perimeter p_{in} of the channel ($p_{in} = 2d + 2w$) is only a few % in the present experiments and is significantly small compared to the change in d, where the plate width w is 26mm. In other words, the meniscus perimeter can be treated as a constant while meniscus curvature is a variable.

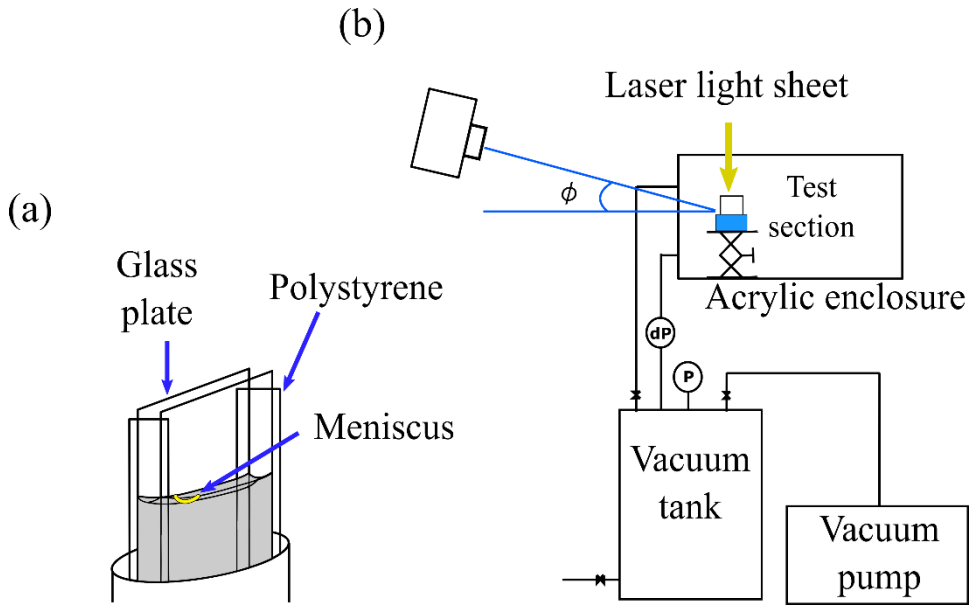

Fig. 2-1. (a) Test section (b) Schematic picture of experimental apparatus

The test section was installed in an acrylic transparent enclosure, as shown in Fig. 2-1(b). The enclosure connects with an auxiliary tank in which air was evacuated prior to the experiments. Both of the enclosure and tank were covered by a thermal insulator. After evacuating air from the tank to a desired pressure, the connecting valve between the enclosure and tank was opened to reduce system pressure in the enclosure. The pressure difference between the enclosure and tank was monitored by a differential pressure gauge (KEYENCE Corp.). The output of the pressure gauge in the pressure equalization is shown in Fig. 2-2. The pressure difference decreased from atmospheric pressure to zero in 1 minute after opening the connecting valve. After the pressure equalization, the differential pressure slightly increased again due to the capillary evaporation of water.

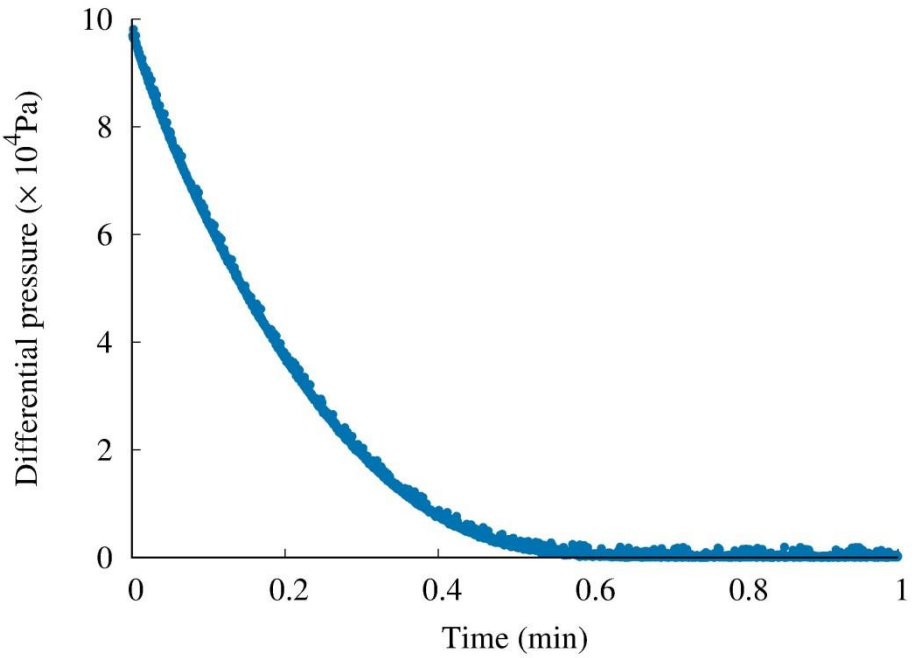

Fig. 2-2. Temporal variation of differential pressure after opening the connecting valve between the enclosure and tank

Because there was no artificial heater in the experimental system, the evaporation is controlled by air-vapor binary diffusion. To evaluate evaporation quantities, the following correlation function was introduced;

$$f(t) = a \times \mathrm{erfc}\left(\frac{b}{\sqrt{t}} \right), \tag{2.1}$$

where a and b are fitting parameters. t is time period after pressure equalization. The pressure equalization was defined as 1 minute after opening the connecting valve. The pressure data were correlated by Eq. (2.1), as shown in Fig. 2-3. The parameters were used to obtain evaporation rates defined as time-differentiation of Eq. (2.1)

$$\dot{m} = \frac{V}{R_v T_v^*} \frac{df}{dt} = ab \frac{V}{R_v T_v^* \sqrt{\pi t^3}} \exp\left(-\frac{b^2}{t} \right), \tag{2.2}$$

where $\dot{m}, V, R_v, T_v^*$ are the evaporation rate, volume of the gas phase, specific gas constant of water vapor, and temperature in the gas phase, respectively. The vapor was assumed as an ideal gas and T_v^* was set to room temperature 22±1℃. The apparent evaporation flux $\dot{m}/A_{cross}$ was defined as the evaporation rate divided by a cross-sectional area $A_{cross} = 2wd$.

The author also analyzed the apparent contact angles of menisci. The quasi-equilibrium 2-dimensional shapes of menisci illuminated by laser light sheet from the top were obtained by a camera (D7100, NIKON Corp.) coupled with the Cassegrain optical system (Seika Corp.). The spatial resolution was 0.9~1.4 μm/pixel. The example was shown in Fig. 2-4. After detecting the contour of meniscus through the image processing, the apparent contact angle (θ in Fig. 2-4) was analyzed by software FAMAS (Kyowa Interface Science Co., Ltd.). Because the camera axis is inclined, the apparent contact angle was corrected with the angle ϕ (see Fig. 2-1(b)). The experimentally-obtained apparent contact angles with various channel sizes are shown in Fig. 2-5. The error of data results from the roughness of the contour. As shown in Fig. 2-5, the apparent contact angles in the present experiments were around 0.6~0.9 rad and not depend on channel size.

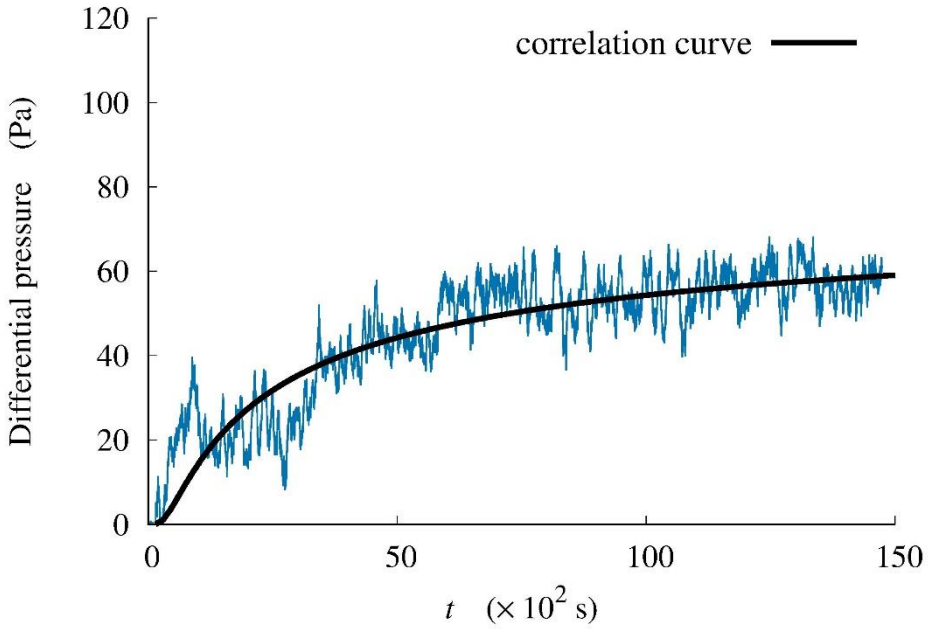

Fig. 2-3. Differential pressure after pressure equalization

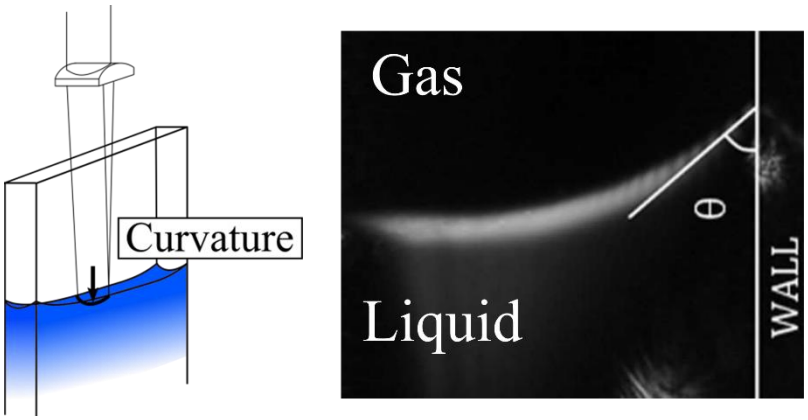

Fig. 2-4. 2-dimentional shape of meniscus near test plate, illuminated by laser sheet

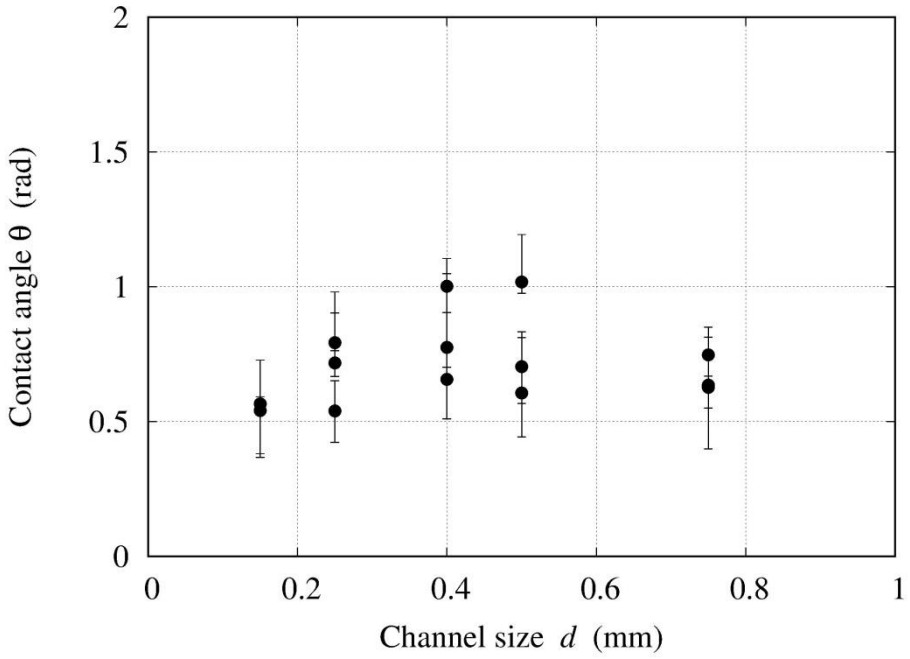

Fig. 2-5. Apparent contact angles of menisci

2.2.2 Evaporation in germanium channels

The test section consists of two test plates and two Polystyrene endplates. The test plates were made of germanium (Furukawa denshi Co., Ltd.) and these surfaces were coated with epoxy-based photoresist SU-8 3025 (Nippon kayaku Co., Ltd.), which enabled to measure the surface temperatures to be mentioned later. The resist surfaces were hydrophilized with a hydrophilic polymer to change the wettability as shown in Fig. 2-6. Prior to the experiments, the test plates were immersed in isopropyl alcohol for a few minutes to remove organic matters. The clean surfaces of disposable Polystyrene end plates prepared by peeling off laminating films prior to the experiments were used. Figs. 2-7(a) and (b) show the rectangle-shaped test section for the evaporation experiments. The plates constituting a channel were fixed at the lower and upper parts of the rectangle tube. The channel size between test plates was adjusted by thickness gauges in the condition of $d < \kappa_{cap}^{-1}$. The change in the inner perimeter p_{in} of the channel can be treated as a constant because of long plate width $w = 30$ mm. The test section was connected with an inlet tube for injecting degassed purified water by a syringe. After a meniscus formed at 10±3mm from channel exit and checking there is no leaking of liquid, the inlet tube was closed to establish a steady-state condition. After removing the syringe from the inlet tube, the liquid remaining between the closed position and the exit was drained.

As mentioned in the next section, the indirect measuring method for the evaporation rate by the temporal variation of system pressure yields big errors. Hence, the author newly introduced the electric balance (EX225D, OHAUS Corp.) for more precise measurements. The conceptual picture of the experimental apparatus is illustrated in Fig. 2-7(c). The test channel was stabilized on the electric balance in an enclosure connected to an auxiliary tank in which the air was evacuated prior to the experiments. By opening the connecting valve, the pressures in the enclosure and the auxiliary tank started to equalize. The equalization was achieved and the output of the balance stabilized in 3 minutes, as shown in Fig. 2-8. The weight of the test section measured every second was used to analyze the evaporation rates by averaging its temporal variation over 10min. The weight decrease is about 6mg in 10min in the present experiments, so the resolution of the balance, 0.01mg, is considered to be sufficient for the measuring. The pressure measured by a pressure gauge (PPX-R01NH-6M, CKD Corp.) was 7.87×10^4 Pa and constant in the measuring period within the error of 0.02×10^4 Pa. The temperature in the test enclosure was 23.5±1.0℃. The outside condition (23.0±1.0℃, 7±4%RH) affects the initial condition and may yield the errors. The preliminary tests were conducted and the evaluated S.T.D. of the evaporation rate was 6%.

The author also conducted supplemental experiments by infrared thermography. As mentioned before, the author used the germanium-based test plate which has high transparency for long-wavelength infrared radiation and is usually used for windows of IR cameras. To measure the surface temperatures of the plates, we coated a photoresist film on the surfaces by means of a spin coater. We used the epoxy-based photoresist SU-8 3025 to make a coating film of 30μm in thickness. As illustrated in Fig. 2-9, the coating film acted as a good IR absorber. This film was formed on the whole inside and half of the outside surfaces to measure the temperature of both surfaces simultaneously. The temperature distribution of the plate in the open air was observed with the IR camera (R500EX, Nippon Avionics Co., Ltd.) with a 52μm lens.

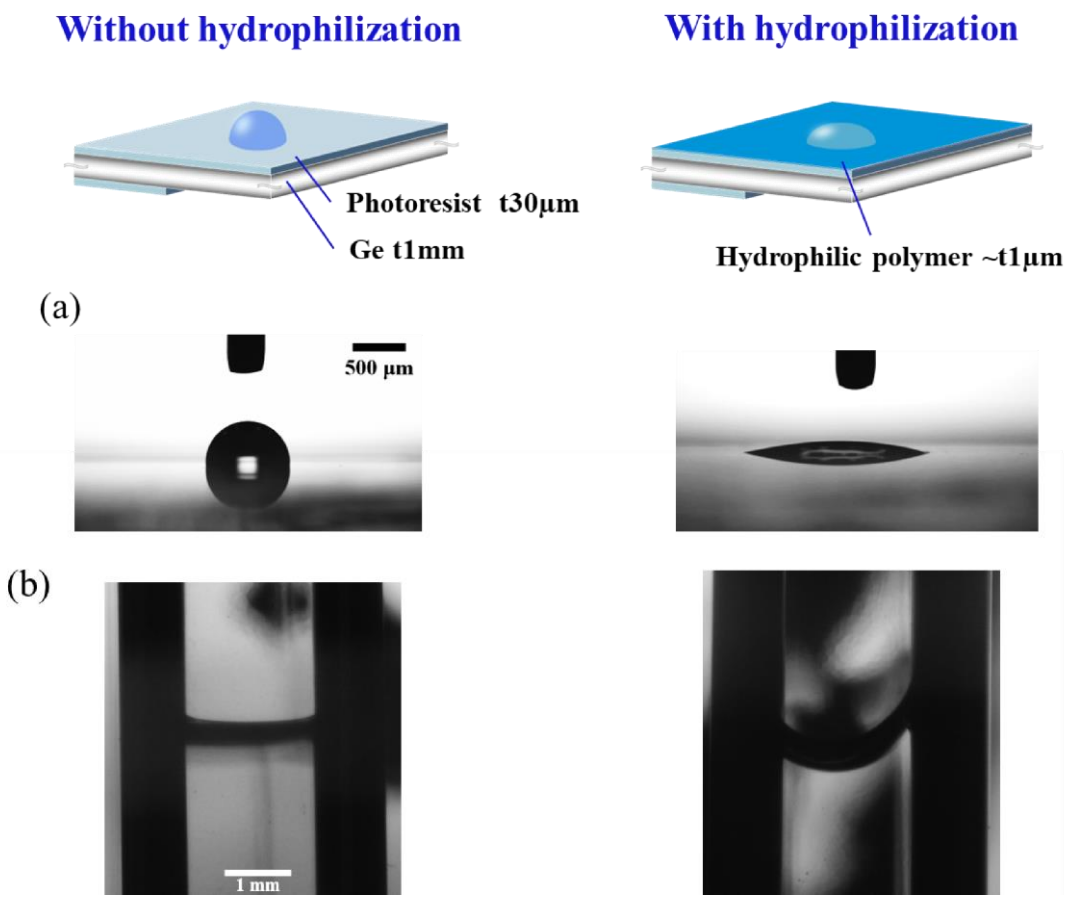

Fig. 2-6. Wettability of test plates with and without hydrophilization (processed by Yoshida SKT Co., Ltd.) for (a) sessile droplet and (b) meniscus in a channel whose size is 2mm. Receding contact angles of evaporating menisci are $\theta = 1.20 \pm 0.14$ rad (without hydrophilization) and $\theta_{left} = 0.853 \pm 0.087$ rad, $\theta_{right} = 0.412 \pm 0.054$ rad (with hydrophilization).

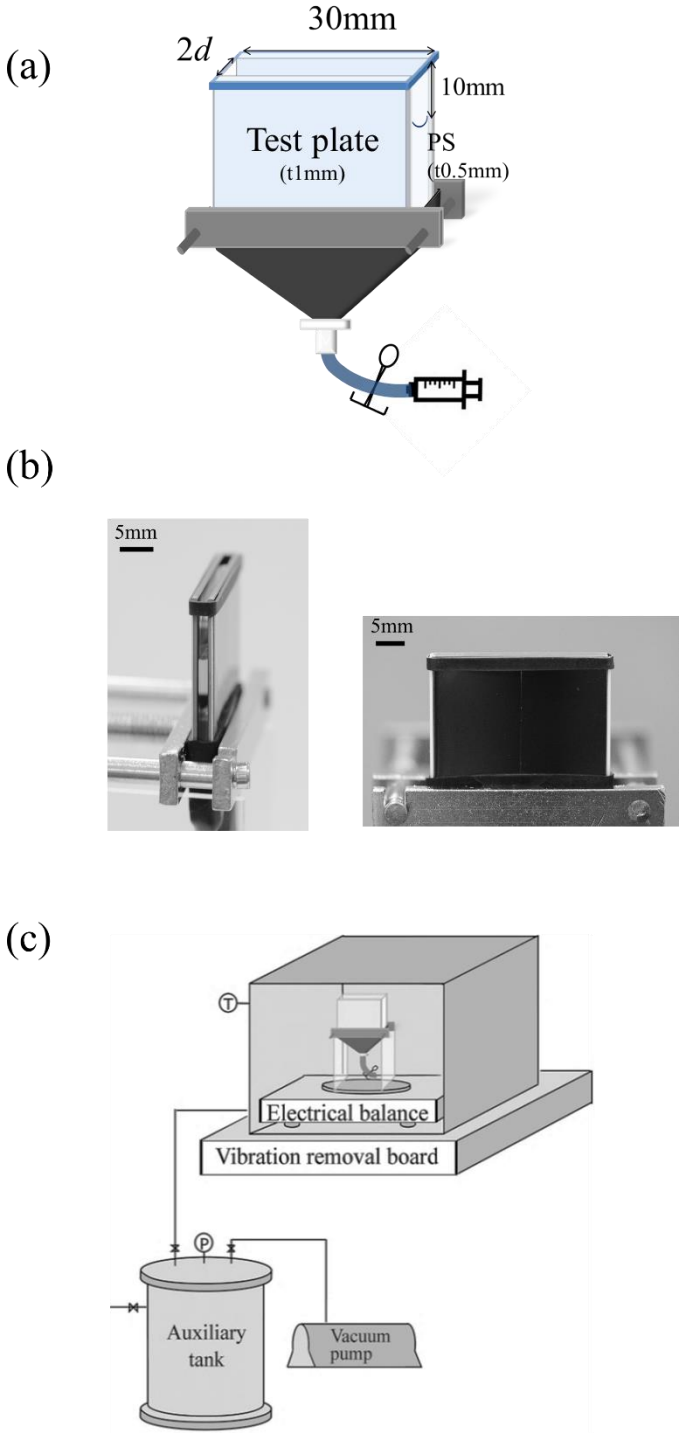

Fig. 2-7. (a) Test section, (b) actual image of test channel, (c) test section and experimental apparatus in measurement for evaporation rates. Experiments were conducted under reduced pressure of 7.87×10^4 Pa.

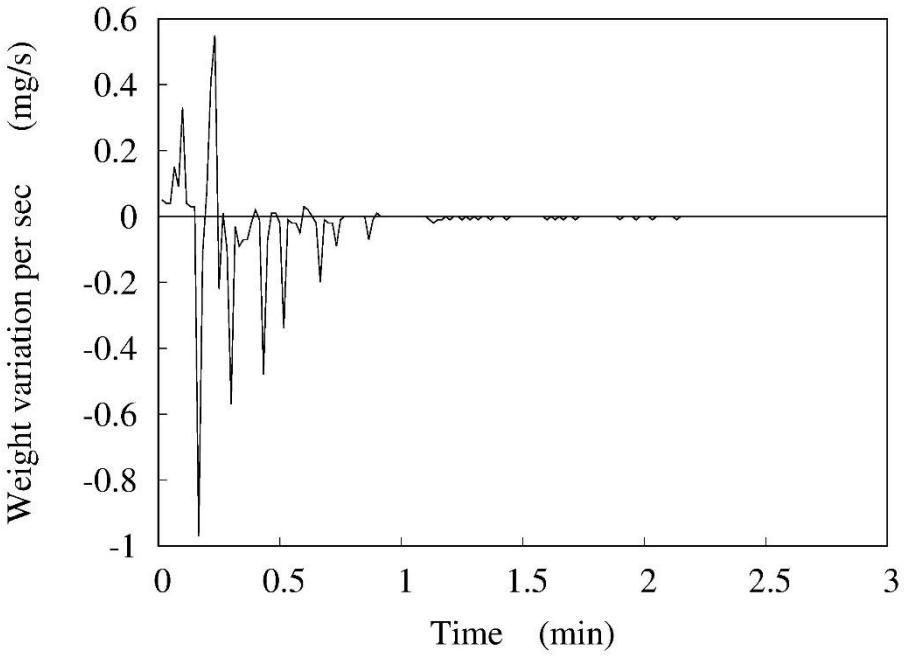

Fig. 2-8. Temporal variation of the weight data after opening the connecting valve

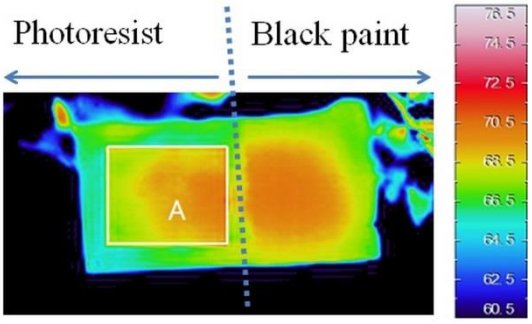

Fig. 2-9. Temperature field of heated SU-8 film (taken by IR camera). Right half of the coating film was black painted. Modified emissivity in rectangle area A surrounded by white line is 0.89.

2.3 Results and discussions on conventional theory

2.3.1 Results of experiments in 2.2.1

Fig. 2-10 shows the evaporation rate $\dot{m}$ and apparent evaporation flux $\dot{m}/A_{cross}$ calculated from the parameters a and b shown in Table. 2-1. The error bars are the standard deviation calculated from the fitting. The evaporation rate and flux in Fig. 2-1 were calculated with $t = 3600$ s when the differential pressure gets close to saturation. The dependence of the evaporation rate on the channel size is different from the previous experiments for capillary tubes [42] in which the rate decrease with reducing tube size. In the present experiments, the evaporation rates are almost constant, or even slightly increase, with reducing channel size. Because the channel area linearly decreases with reducing channel size, the significant apparent evaporation flux was found in the narrower channel. The flux of the 0.30mm case was about 40 times larger than that of the 1.50 mm case. Fig. 2-11 shows the apparent evaporation flux with interface curvature κ defined as $\kappa = \cos\theta/d$. Because the apparent contact angle is almost constant with channel size, the apparent flux increased with increasing interface curvature.

Table 2-1. Fitting parameters

	d=0.75mm	0.50mm	0.40mm	0.25mm	0.15mm
a (Pa)	28.9	58.3	77.8	91.9	97.8
S.T.D *a* (Pa)	10.1	21.3	32.0	36.3	8.62
b ($s^{1/2}$)	13.0	16.1	17.9	28.8	36.6
S.T.D *b* ($s^{1/2}$)	4.65	13.3	9.30	5.17	0.928

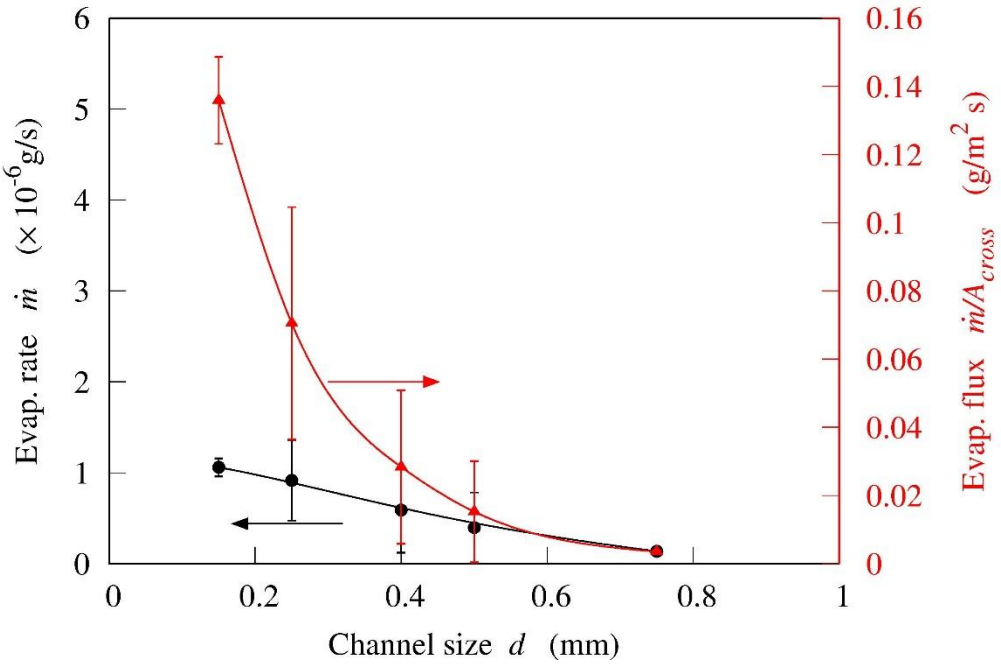

Fig. 2-10. Evaporation rate and flux at $t = 3600$ s calculated with parameters a and b shown in Table 2-1.

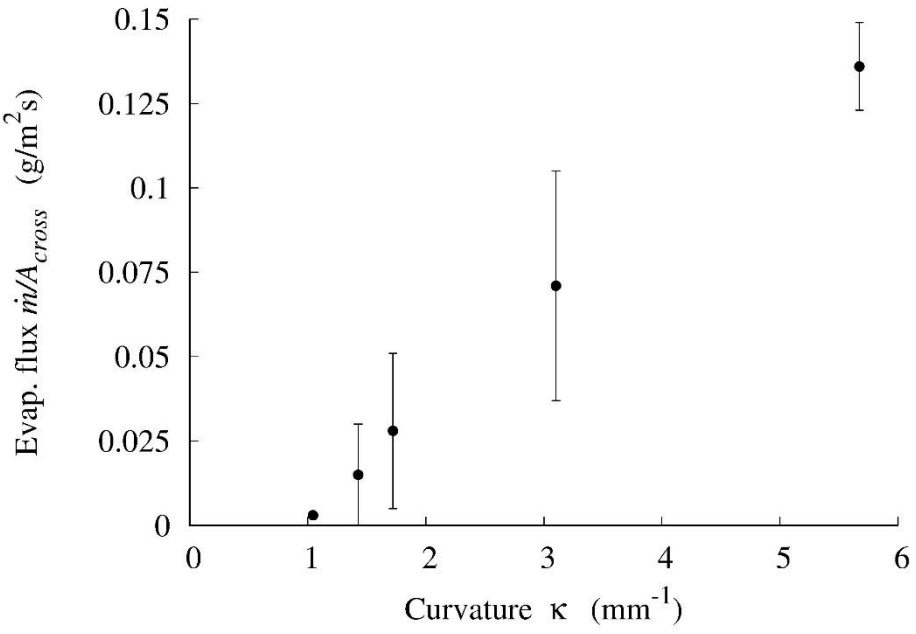

Fig. 2-11. Apparent evaporation flux at $t = 3600$ s vs interface curvature

Fig. 2-12 shows the apparent evaporation fluxes obained in the present experiment and previous experiments [42] where organic volatile liquid (Ethanol, Methanol, Acetone, and Pentane) evaporated to open-air from capillary tubes. The area-averaged flux in the previous experiments was converted to apparent flux by assuming the interface shape as a spherical cap. These experiments show the same tendency that narrower channel size, or larger interface curvature, exhibits higher evaporation. It is notable that the previous experiments were conducted in open-air while water evaporated in reduced pressure in the present experiment. This difference in the boundary condition may be the reason why the flux of water in this experiment is comparable to that of the volatile liquid.

As discussed in Section 1.3, Buffone & Sefiane proposed that the evaporation rate is a function of contact-line length. It predicts the evaporation flux monotonically increases with reducing channel size. Fig. 2-13 shows the apparent evaporation fluxes plotted with the inner perimeter p_{in} of the channel and capillary tube. In the previous experiments, the evaporation flux of volatile liquid increases with reducing channel size. However, if the evaporation flux is a function of only contact-line length, it leads to the unphysical result, the volatility of water would be much greater than that of volatile organic liquid. This is obvious if the evaporation flux is extended to $p_{in} \to 0$. The difference is significant even considering the difference in the boundary condition. This result implies the evaporation kinetics may strongly depend on the characteristic length of the meniscus, or interface curvature.

It must be noted that the above discussion is limited to near saturation state. As clearly shown in Fig. 2-14, these data become scatter before the experimental system reached saturation. It is because the resistance between the source and the detector was not constant in this experiment. It does not mean the channel size affects the resistance via Knudsen diffusion because Knudsen number in the channel is about 10^{-3} which is enough small to assume vapor flow as a continuum. The detailed mechanism in this behavior of the resistance is unclear but the essential problem may lay on the indirect measurement technique for evaporation quantity. Hence, the precise direct measurement technique was used in the next experiments, whose results are discussed in the next section.

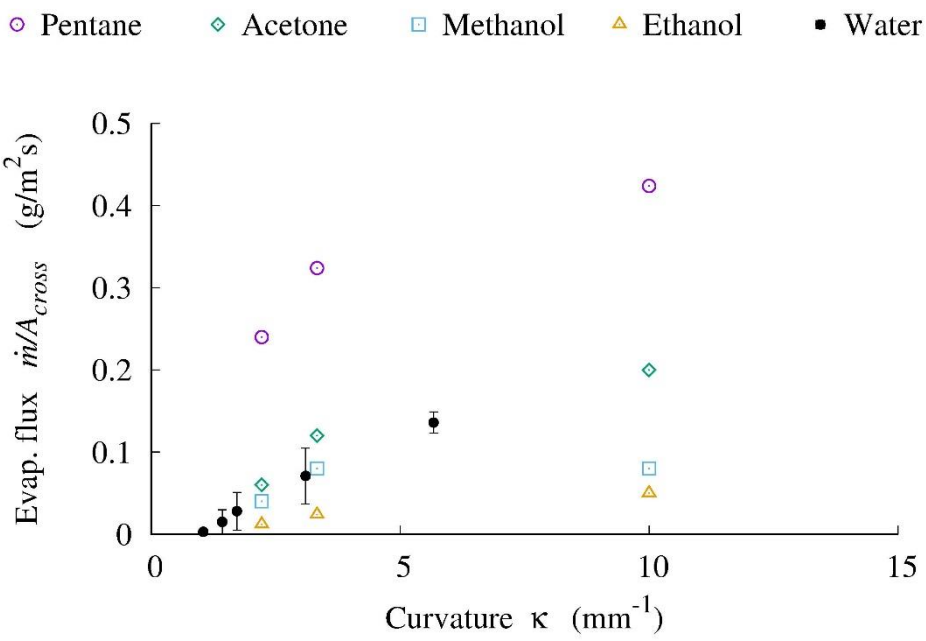

Fig. 2-12. Apparent evaporation flux in present (t = 3600 s) and previous experiments to interface curvature

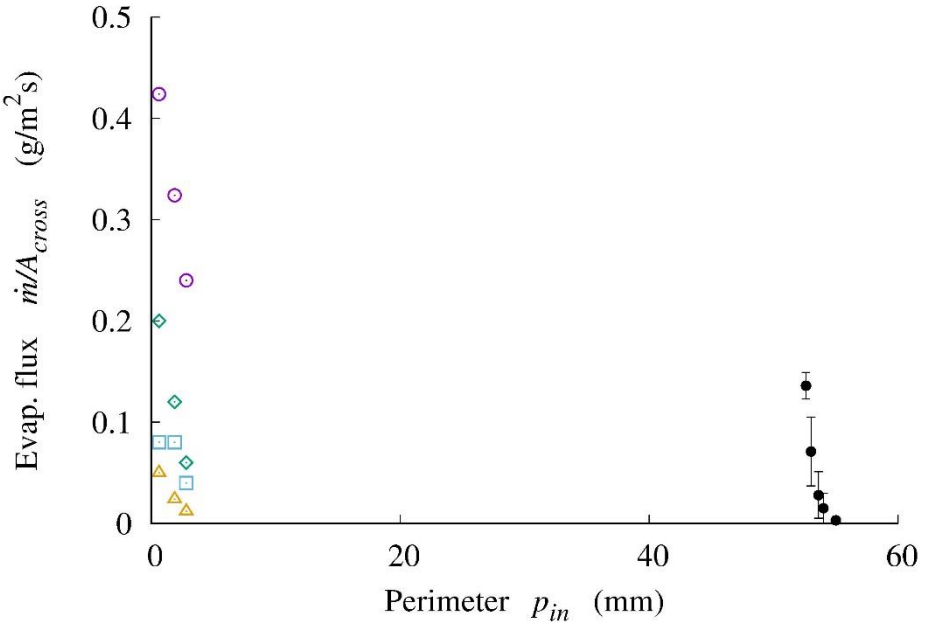

Fig. 2-13. Apparent evaporation flux in present (t = 3600 s) and previous experiments to inner perimeter

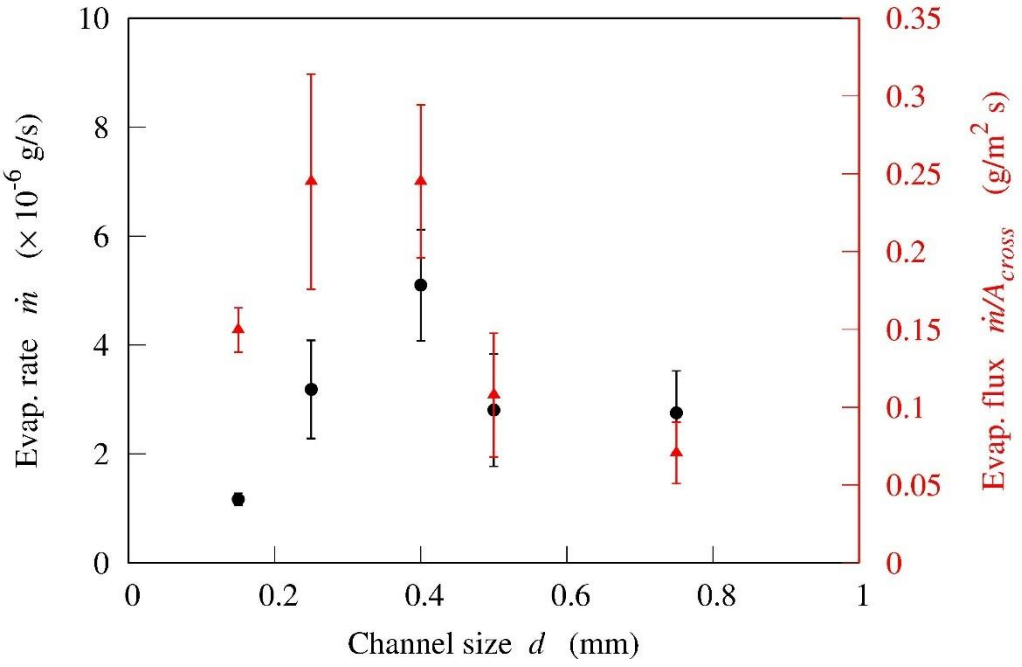

Fig. 2-14. Evaporation rate and flux at $t = 360$ s

2.3.2 Results of experiments in 2.2.2

Experimental data for evaporation rates are tabulated in Table 2-2 and the apparent evaporation flux versus the meniscus curvature is shown in Fig. 2-15. It is observed that the evaporation flux increased with reducing channel size and increasing curvature, which is consistent with the results mentioned above. Fig. 2-16 shows the temperature distribution of the inner and outer surfaces of the channel. In contrast to the previous studies (e.g. [37]), the temperature drop near the contact line was not observed, which may be because the volatility of water is not high and the vapor diffusion layer limits the process. The author conducted an additional experiment to remove the vapor diffusion layer by continuously blowing air. In this case, it was found that the temperature slightly dropped at the 3-phase contact line. On the other hand, if there was a diffusion layer without blowing air, the temperature drop near the contact line was not observed. These results show that the temperature at the wall surface can be assumed to be constant.

Table 2-2. Evaporation rates ($\times 10^{-5}$ g/s) obtained by experiments

	d = 1.02mm	0.76mm	0.38mm	0.16mm
With hydrophilization	1.15	1.02	1.08	1.12
Without hydrophilization	1.03	0.957	0.762	0.850

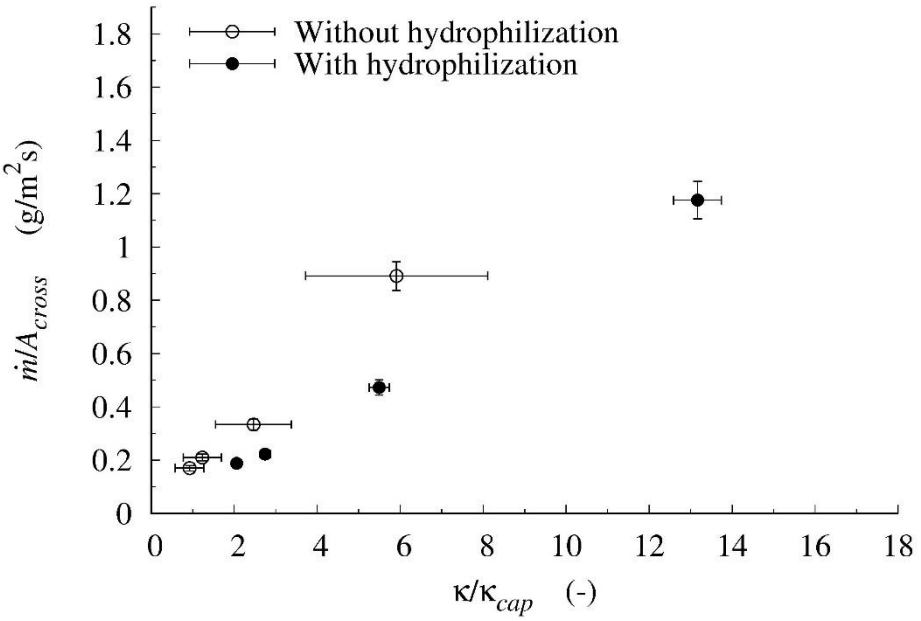

Fig. 2-15. Evaporation flux versus interface curvature. Error bars show standard deviation of evaporation flux for *y*-axis and contact angle for *x*-axis.

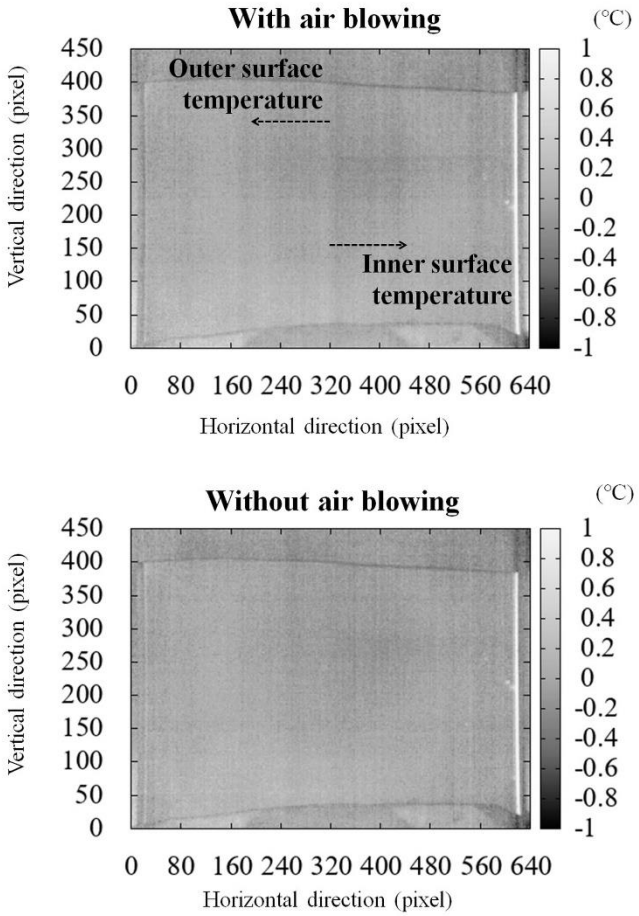

Fig. 2-16. Thermal images minus averaged outer temperature with and without blowing air. Contact line exists at ~280 pixels on vertical axis.

2.4 Summary

The experiments were conducted to investigate the effect of meniscus curvature on evaporation flux. The rectangle channel was used as a test section to distinguish the effect of meniscus curvature from that of the perimeter. The apparent evaporation flux was found to increase with reducing channel size and with increasing interface curvature. This trend is consistent with previous experiments where volatile organic liquid evaporated from capillary tubes. The remarkable result is that present data cannot be explained with the theory which shows evaporation flux is a function of contact-line length. This implies the evaporation kinetics may strongly depend on the characteristic length of the meniscus, or interface curvature. In addition, the separate experiments were conducted to know the temperature of solid surfaces when meniscus evaporates. The surface temperature measured by the IR camera was almost uniform in the presence of the vapor diffusion layer.

Chapter 3 Experiments for perimeter effect

3.1 Introduction

This chapter describes 2 experimental works for evaporation kinetics in various geometrical channels. In the previous chapter, only characteristic length of a meniscus was a variable by choosing rectangle channel size in the condition of $d \leq \kappa_{cap}^{-1}$. In the present chapter, circular and rectangle channels were used to know the size-dependence of the evaporation flux in the condition of $d > \kappa_{cap}^{-1}$ as well as $d \leq \kappa_{cap}^{-1}$.

3.2 Experimental apparatus and measuring techniques

3.2.1 Evaporation in round- and rectangle-shaped channels

The circular and rectangle channels made of glass were used as test sections. These gap conditions are illustrated in Fig. 3-1(a). These two types of geometrical gap configuration are easy to set the perimeter p_{in} and curvature κ of the meniscus by adjusting d which is defined as the inner radius of the circular opening or half-gap-distance between parallel test plates. In the case of $d > \kappa_{cap}^{-1}$ (2.66mm in the present experiments), the characteristic length of an isolated meniscus is κ_{cap}^{-1} [46], which means that meniscus curvature is a constant while the meniscus perimeter is a variable. On the other hand, if d is smaller than κ_{cap}^{-1}, the meniscus curvature becomes dependent on the channel size d. The perimeter could be treated as a constant for rectangle channels having high aspect ratios, as mentioned in the previous chapter. In this case, the meniscus can be approximated as a spherical cap for a tube [42] and a part of the cylindrical side for a rectangle channel, which enables to analyze the meniscus curvature κ and interface area A_i. Table 3-1 summarizes the experimental conditions of each test section. As tabulated in Table 3-1, the author used the round-shape petri dishes (AS ONE Corp.) and the tubes (AS ONE Corp.) for circular channels, and the disposable parallel glass-plates (Muto Pure Chemicals co., ltd.) with the Polystyrene ends for rectangle channel. The latter is the same configuration presented in the previous Section 2.2.1 except for the plate width w. In the present experiments, the plate width w was set 13, 26 and 40mm. These w values were chosen based on the maximum weight on the electric balance mentioned before.

Prior to the experiments, all test sections were rinsed with ethanol (99.5 wt.%, Hayashi Pure Chemical Ind., Ltd.) and purified water and then dried in atmosphere. The degassed purified water

was gently poured to the pool in which the tubes and parallel plates were stably set in the purified water pool. The meniscus is formed by capillary action at an equilibrium position in the channel. To prevent evaporation from the pool surface except for the menisci in the confined geometries, rapeseed oil having small vapor pressure was floated on the pool surface. In the petri-dish case, the effect of the heat conduction from the bottom substrate of test sections may appear if the liquid height is less than the order of a micrometer, hence the liquid height was kept more than 6mm in every case.

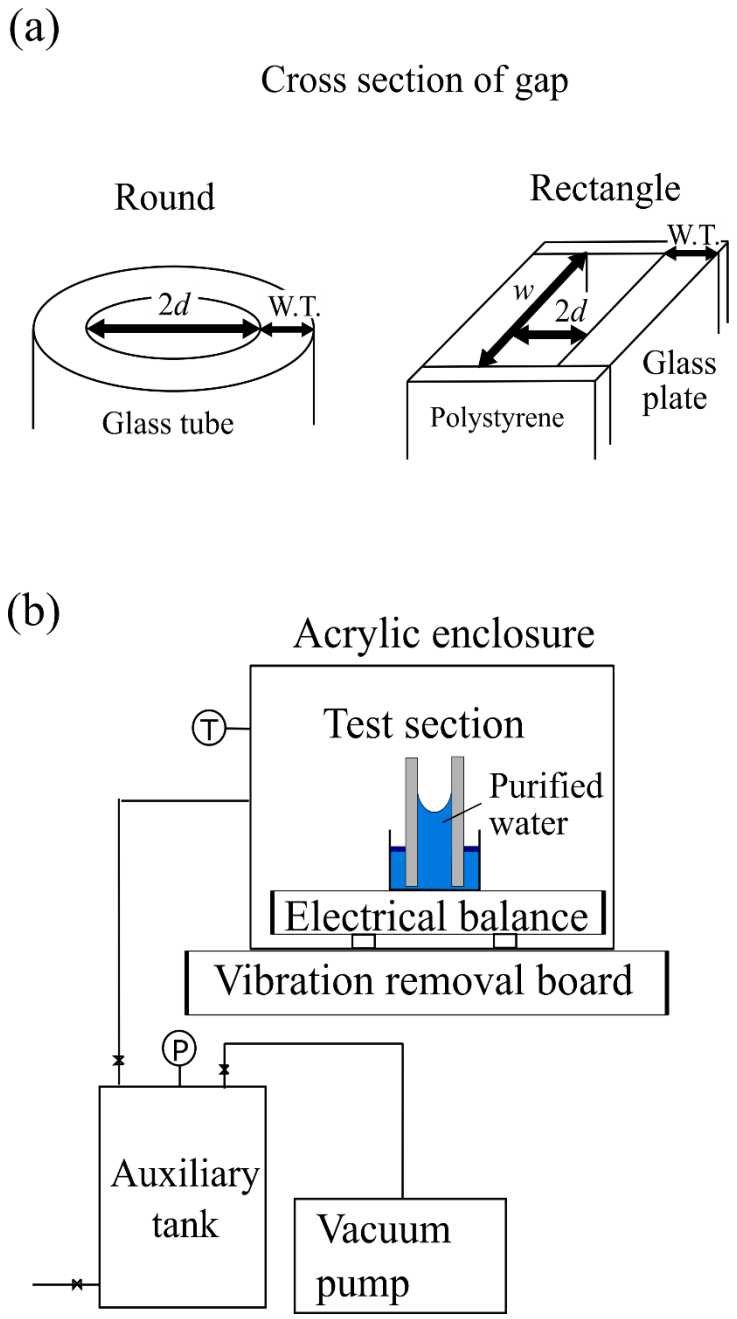

Fig. 3-1. Schematic diagrams of (a) gap configurations and (b) experimental apparatus.

Table 3-1. Summary of characteristic length of channel size d, static contact angle θ and wall thickness (W.T.)

	Petri dishes			Tubes			Plates
d [mm]	13.30	29.25	43.63	1.00	1.98	2.95	0.15~3.00*
θ [deg]	20.3	28.7	18.4	36.7	41.8	43.7	10.2, 8.6, 2.7**
W.T. [mm]	1.95	2.10	2.43	1.00	1.03	1.05	1.00

* Set by thickness gauges. ** These contact angles correspond to three plate widths: 13, 26 and 40mm, respectively.

The conceptual picture of the experimental apparatus is illustrated in Fig. 3-1(b). The experimental apparatus and measuring procedure are the same as Section 2.2.2. The test channel was put on the electric balance in an enclosure connected to an auxiliary tank in which the air was evacuated prior to the experiments. By opening the connecting valve, the pressures in the enclosure and the auxiliary tank started to equalize. The equalization was achieved and the output of the balance stabilized in 3 minutes. The weight of the test section measured every second was used to analyze the evaporation rates by averaging its temporal variation over 10min. The resolution of the balance was 0.01mg. The minimum weight decrease is about 0.3mg in 10min. The pressure measured by a pressure gauge (PPX-R01NH-6M, CKD Corp.) was 7.88×10^4 Pa and constant in the measuring period within the error of 0.02×10^4 Pa. The temperature in the test enclosure, measured with K-type thermocouple and data logger (34972A, Keysight), was also constant at 22.1℃. The standard deviation is ±1.0℃. Because the experimental system was enclosed with a thermal insulator, the outside environment (20.0 ± 1.0℃, 28.0 ± 15.5%RH) affected the initial condition. The standard deviation of the evaporation rate evaluated by preliminary tests was 6%.

θ in Table 3-1 represents the static contact angles of menisci in the tubes (see Fig.3-2(a)) and of the droplets on the petri dishes and test plates measured by DM-300 (Kyowa Interface Science Co., Ltd.) in open-air. The refraction effect on the meniscus in the tube was corrected considering the curvatures of the tube wall. The heights of the droplets (maximum 0.33mm) on the dishes and the plates were smaller than κ_{cap}^{-1}, which ensures that the gravity effect was negligible. However,

it did not ensure that the contact angles of droplets and menisci were identical. If these are not identical, the difference may lead to erroneous evaluation of interface curvature κ. Therefore, the supplementary experiments were carried out to measure the contact angles of menisci in rectangle channels by the laser interferometry which has been used for visualizing microscale liquid film under the nucleate boiling bubble [47]. The laser light sheet (the wavelength $\lambda_w = 450$ nm) horizontally irradiating the meniscus (refractive index $n_\ell = 1.33$) with the given incident angle of $\pi/4$ interfered with the reflection from the gas-liquid interface. The bright fringes appeared as the results of the interference, as shown in Fig. 3-2(b). The interference fringe spacing corresponding to $\lambda_w / 2n_\ell \cos\theta_\ell$ [47], where θ_ℓ is the angle of refraction into the liquid from solid, was observed by a camera coupled with the Cassegrain optical system. The maximum resolution of the observed image was 0.84μm/pixel. To prevent the reflection at the outer surface of the test plate, a right-angle glass-prism was put on the outer surface and the gap between the glass surfaces was filled with silicon oil. Although the spatial resolution of this interferometry is not as good as the technique developed by Wayner and coworkers [24,26,28,48,49], which covers the adsorbed film to a few micrometers, this method is enough to achieve the purpose for evaluating the apparent contact angle defined as a gradient of the interface at outer edge of micro region (≈ 1μm).

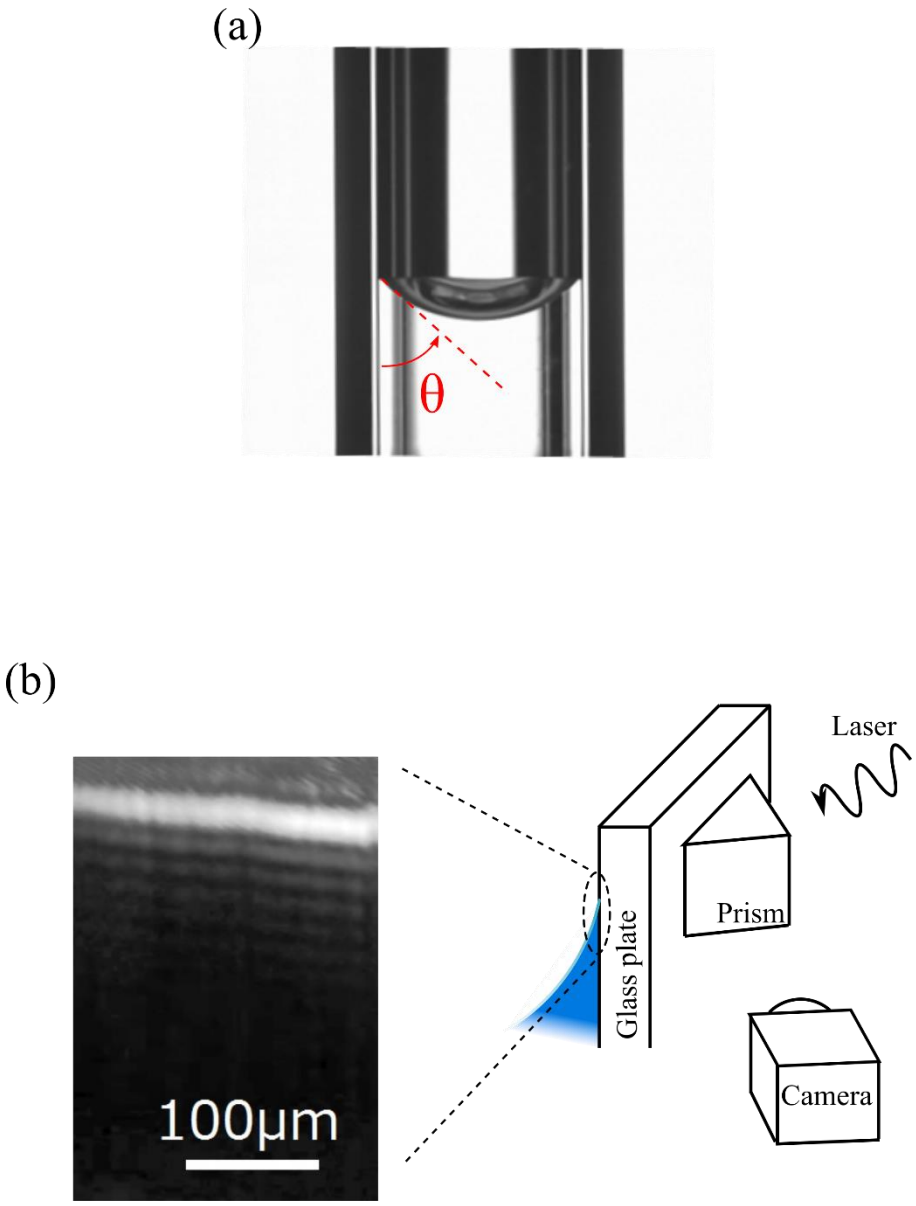

Fig. 3-2. (a) Contact angle measuring for capillary tube (b) Interference fringes observed by interference technique

The effects of chemical and physical impurities on the interference fringes should be mentioned. For chemical impurities, the oil floating on the pool surface may become the possible source, but the author believes the effects of oil are not significant for the following reason. To qualitatively know how the chemical impurities affect the measurements, consider the impurities diffusing from the source (oil) and coming into the meniscus. Because the impurities are not volatile, these should be accumulated at the interface, mainly three-phase contact line on the glass plate whose surface energy is high. The impurities act to make the surface energy lower and the contact angle higher. Hence, the contact angles should increase with time, if the assumption was correct. In fact, however, such temporal behaviors were not observed. On the other hand, as for the effect of physical impurities, the measurement could be affected in different ways. In the previous studies by Panchamgam et al. [26,27,50,51], the total system was enclosed by a clean glove box to avoid contaminants affecting the fringes, whereas the system in these experiments potentially includes the particles naturally existing in the surrounding environment. If the particles adhere to the surfaces, the interference fringes become nonparallel in some regions [24], which causes some errors in measurements. Hence, the parallel fringes are used for the following analysis to avoid the effect of these particles. It must be noted that the presence of particles also affects the wetting physics. Panchamgam et al. [28] studied the effect of impurities on the evaporating menisci and showed that the adsorbed film thickness and the dispersion constant become thicker and smaller in the presence of nanoparticles, which slightly deviates the wetting condition from the ideal 3-phase system. However, the latter case could not affect the result in these experiments because all experimental condition is the same.

3.2.2 Evaporation in cuvettes

This section describes supplemental experiments to demonstrate the geometrical dependence of evaporation flux changes around $d = \kappa_{cap}^{-1}$. The author used borosilicate glass cuvettes which have 4 different channel sizes $2d$ of 10mm, 5mm, 2mm, 1mm, as shown in Fig. 3-3(a). The channel width and wall thickness are 10mm and 1.25mm, respectively. The working fluid was IPA (99.7 wt.%, Hayashi Pure Chemical Ind., Ltd.) whose capillary length is 1.66mm at 298K. In other words, 10mm and 5mm cases correspond to the condition of $d > \kappa_{cap}^{-1}$, and 2mm and 1mm cases correspond to $d < \kappa_{cap}^{-1}$. Because the glass surface has high surface energy, IPA film extremely extends at the 4 corners of the channel. To reduce the effect of a corner, the cuvette surfaces were coated with fluorine resin (FC-250, Fine Chemical Japan Co., Ltd.). The wetting condition changes to partially-wetting (40.9±5.3deg. of equilibrium contact angle) for 1μL IPA droplet on slide glass

due to this coating. The effect of corner can be effectively reduced because the wetting condition drastically changed and the corners were filled with the resin. The cuvettes were filled with purified water and capped to avoid contamination while stored.

Prior to the experiments, water in the cuvettes was drained and ethanol (99.5 wt.%, Hayashi Pure Chemical Ind., Ltd.) was poured. Next, ethanol in the cuvettes was drained and the remaining ethanol droplets were removed by heating. After the cuvettes cooled to room temperature, IPA was gently injected by a syringe along the cuvette corner to the desired position. If there were no remaining droplets above the meniscus, the cuvettes were capped and placed in a grove box. The pressure and ambient temperature in the grove box were atmospheric pressure and 297K, respectively. The humidity was controlled to 0% to prevent IPA from absorbing water vapor. After starting the experiment with simultaneously opening the 4 cuvettes to allow the liquid naturally evaporating, each meniscus position was captured by a camera at 1min intervals. Finally, image processing was performed to analyze the receding distance of the bottom of the meniscus from its initial position. According to the series of the image, the meniscus kept its shape in receding. The inset of Fig. 3-3(b) shows the meniscus formed at the corner of the channel. The image demonstrates that the extended liquid film at the corners may be negligible.

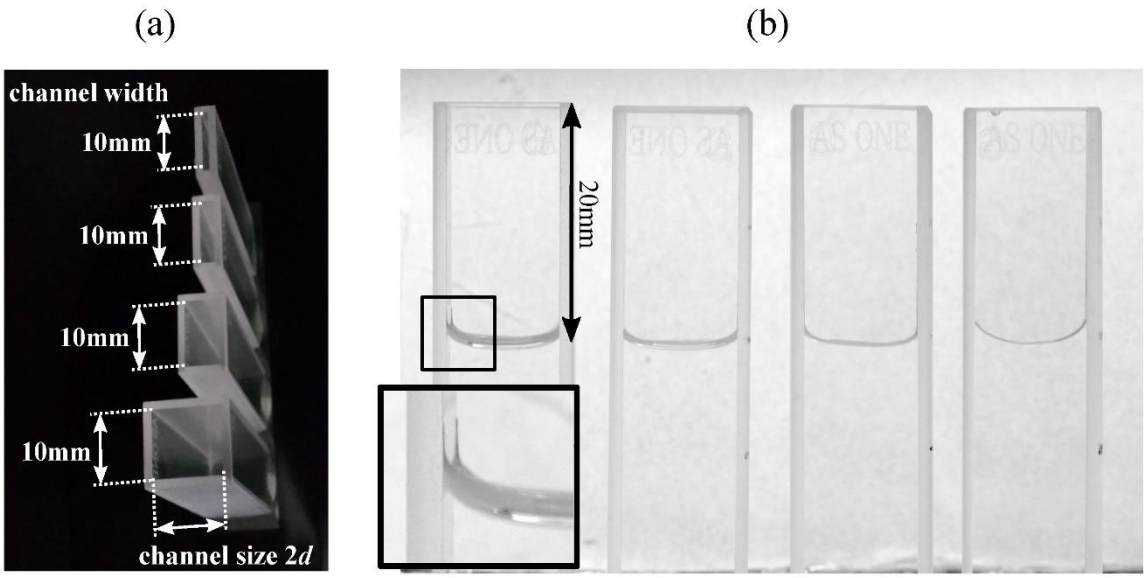

Fig. 3-3. (a) Test cuvettes having 4 different channel sizes $2d$ of 10mm, 5mm, 2mm, 1mm.
(b) Menisci formed in channels ($2d$: 10mm, 5mm, 2mm, 1mm from the left)

3.3 Results and discussions

3.3.1 Results of experiments in 3.2.1

Fig. 3-4(a) shows the liquid film profile obtained by the laser interferometry prior to the evaporation experiment. The coordinate origin was set at the brightest fringe, i.e., 0th order fringe. The film thickness monotonically increases with respect to a downward direction along the wall surface. The gentle slope at the low order (0th and the next fringes) maybe because of disjoining pressure which acts to thicken the wetting film [52]. Generally, the effect of disjoining pressure appears in the film of which thickness is less than 1μm [20], hence, the slope in the region ~1μm is considered to represent the apparent contact angle. Hence, θ was evaluated by linear-fitting the film profile from 0.86μm to 1.72μm (the maximum thickness which can be observed); for instance, apparent contact angle in Fig. 3-4(a) is $0.887° \pm 0.013°$. Since it was observed that the meniscus shape kept the same during the experiment, θ was found to unchange with experimental time, as shown in Fig. 3-4(b).

Fig. 3-5 shows the apparent evaporation flux $\dot{m}/A_{cross}$ of various geometrical gap configurations, where A_{cross} is a horizontally-projected interface area. The horizontal axis is the inner perimeter p_{in} of the channel. The flux increased with reducing p_{in}, as reported in the previous study [43], however, the dependence of the flux on the geometrical configuration is different whether the channel size d is greater than or less than capillary length κ_{cap}^{-1}. In the case of $d > \kappa_{cap}^{-1}$, the flux slightly increased with reducing p_{in}. Once d became less than κ_{cap}^{-1}, the evaporation flux sharply increased and branched into $d > \kappa_{cap}^{-1}$ and $d \le \kappa_{cap}^{-1}$. The increase and the branching of the evaporation flux for $d < \kappa_{cap}^{-1}$ may show that the main factor of evaporation switched from the perimeter to the meniscus curvature.

It must be noted that the cases of $w = 13\,\mathrm{mm}$ were excluded in the discussions. Fig. 3-6 shows the relative variations of evaporation flux with different w at constant d. It can be found that the evaporation flux increases at $w = 13\,\mathrm{mm}$ while the cases at $w \ge 26\,\mathrm{mm}$ are almost constant. In addition, the increase in the flux was found to be significant with reducing d. This behavior may be due to the presence of sharp ends in the gap. If the interface area at these ends does not depend on channel size, the ratio of the end area to the total interface area increases with reducing d. Since this study did not focus on this end effect, the cases of $w = 13\,\mathrm{mm}$ were excluded in the discussions.

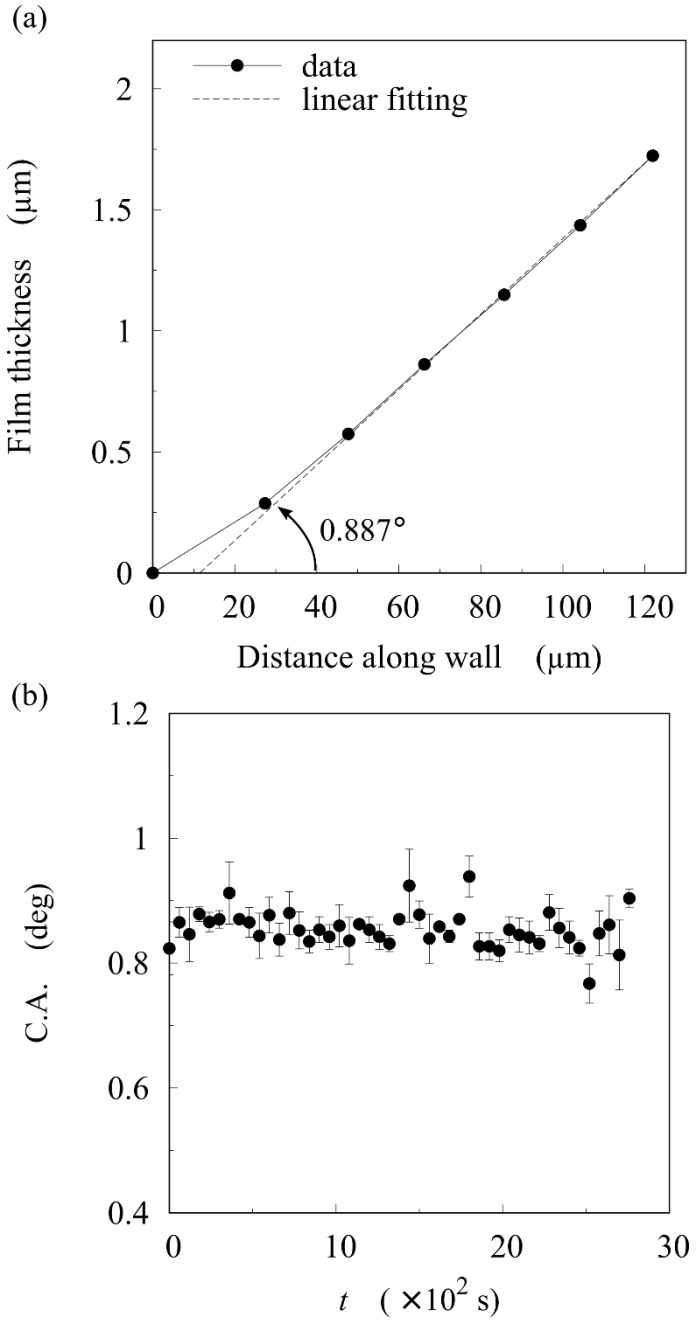

Fig. 3-4. (a) Liquid film profile in parallel plates ($d = 0.40\,\text{mm}$, $w = 26\,\text{mm}$)
(b) temporal variation of contact angle

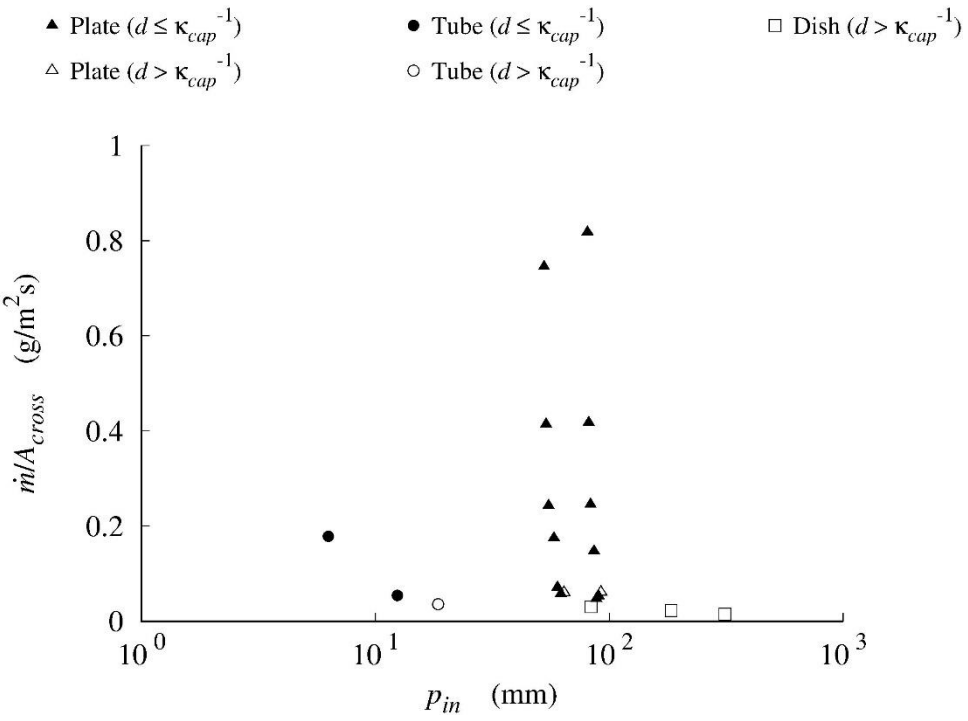

Fig. 3-5. Apparent evaporation flux versus perimeter

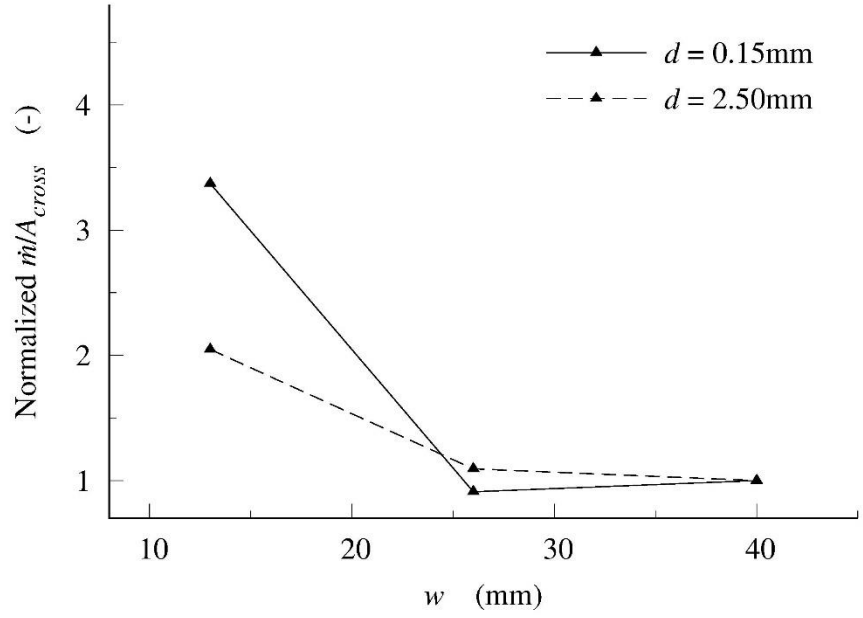

Fig. 3-6. Apparent evaporation versus plate widths

Fig. 3-7 shows the apparent evaporation flux versus $p_{in}\cos\theta/A_{cross}$ which corresponds to the ratio of the contact area to the total interface area. In the petri-dish case, the static contact angle of the sessile droplet was substituted because it was difficult to directly measure the meniscus contact angle in this case. The apparent evaporation flux for $d > \kappa_{cap}^{-1}$ was found to slightly increase with the increase in $p_{in}\cos\theta/A_{cross}$, which implies strong evaporation at the contact area relative to the planer interface. The relative increase in the contact area resulted in a slight increase in evaporation flux for $d > \kappa_{cap}^{-1}$. This increase is represented by the straight line in the graph. Once the menisci interfered with each other at $d = \kappa_{cap}^{-1}$ and the interface curvature became greater than the inverse of the capillary length, the evaporation flux sharply increased.

Fig. 3-8 shows area-averaged evaporation flux with interface curvature normalized by κ_{cap}, where interface area A_i was evaluated by approximating spherical or cylindrical interface shape. Although the perimeters for the circular (tube) and rectangle (parallel plate) channels are ten times different, the data for $d \le \kappa_{cap}^{-1}$ is on one curve. The result that area-averaged evaporation flux increased with the interface curvature is consistent with the experiment presented in the previous chapter, but it is found that the inner perimeter is not an important factor for $d \le \kappa_{cap}^{-1}$.

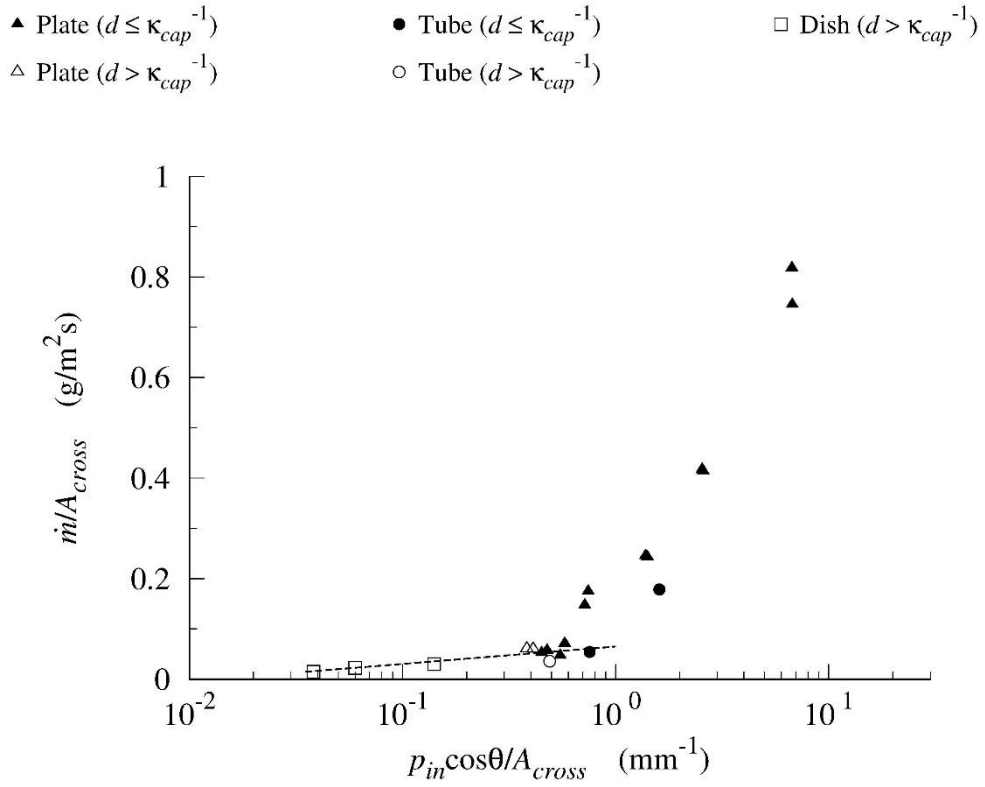

Fig. 3-7. Apparent evaporation flux versus ratio of meniscus area to total area

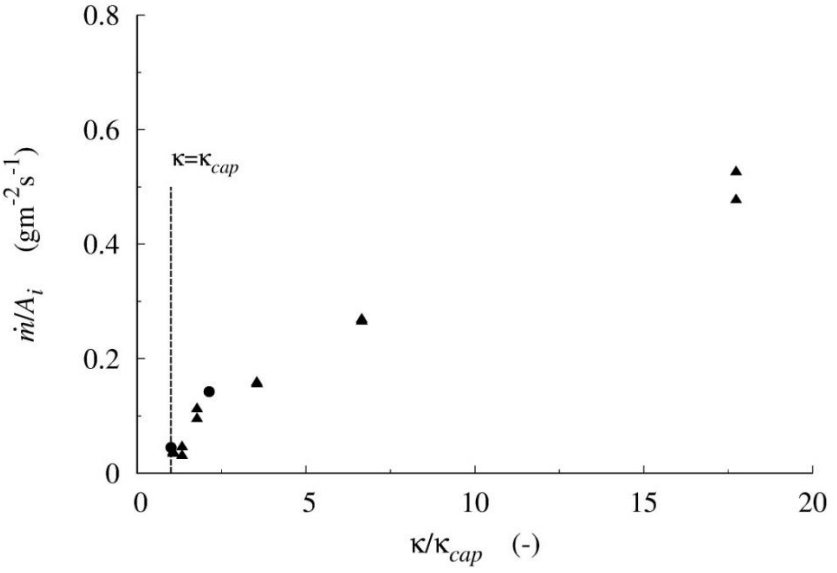

Fig. 3-8. Area-averaged evaporation flux versus interface curvature

The author also conducted the supplemental experiments for temperature measurement near the evaporating interface using a miniature thermocouple. T_ℓ^*, the liquid temperature in evaporating meniscus formed in the rectangle channel was measured with a K-type 25μm-diameter miniature thermocouple (TC) and logged by the data logger (34972A, Keysight). This TC was fixed at the bottom of the test section and the tip was positioned in the liquid phase at the contact region. The TC-tip position was observed by a camera facing to the glass plate surface. The light and black fringes appeared due to the light from a metal halide lamp, whereby it is clear whether the TC in the meniscus touched and deformed the receding meniscus due to evaporation (see Fig. 3-10). T_{ow}^*, the temperature of the outer (gas-side) surface of the channel and T_v^*, the air-vapor mixture in the enclosure were also measured with the K-type 125μm-diameter TCs. The TC-tip for T_{ow}^* was set at the same height of the TC for T_ℓ^* (the maximum error is ~500μm) and covered by the insulator to avoid the effect of gas-phase temperature. The TC position of T_v^* is far from the channel. The evaporation rate of the meniscus was simultaneously measured by the electrical balance. To avoid the TC effects on the resulting evaporation rate, the TCs for T_ℓ^* and T_{ow}^* were fixed at the bottom of the test section, and the large fluctuations of the weight data were removed. The experimental method and boundary conditions are the same as mentioned in Section 3.2.1.

The initial temperatures T_ℓ^*, T_{ow}^* and T_v^* before experiments were 293.1K, 294.2K and 295.1K, respectively. These temperatures decreased in the pressure equalization process, especially T_v^* sharply decreased to 287.6K which in turn recovered to 295.0K by the large heat capacity of the enclosure. Fig. 3-9 shows the temporal variation of T_ℓ^*, T_{ow}^* and T_v^* after the pressure equalization. In the figure, the temperature measurements in the liquid film and at the outer (gas-side) surface of the plate showed the evaporation make T_ℓ^* lower than T_{ow}^*, and the temperatures gradually increased as time progressed. The temperature of the air-vapor mixture T_v^* was higher than T_ℓ^* and T_{ow}^*.

Fig. 3-10 shows temporal variations of evaporation rate with and without TC. This figure shows the effect of TC on the evaporation. The TC for T_ℓ^* in the meniscus touched and deformed the receding meniscus after $t = 4.8 \times 10^3$ s. There is no significant change in the temperatures, while the evaporation rate in Fig. 3-10 significantly increases by 30-40%. In other experiments, the 20-30% increase in the evaporation rate was often observed. This result may support this study's claim that the curvature enhances evaporation.

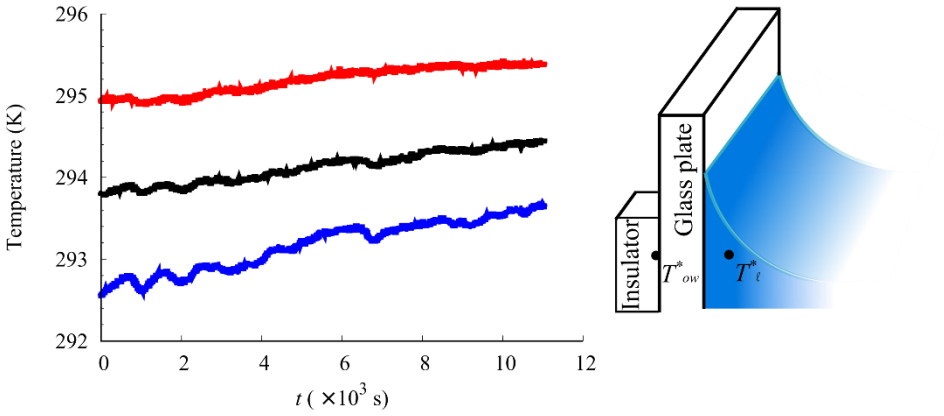

Fig. 3-9. Temporal variation of T_{ℓ}^{*} (blue), T_{ow}^{*} (black) and T_{v}^{*} (red) for $d = 0.40\,\mathrm{mm}$

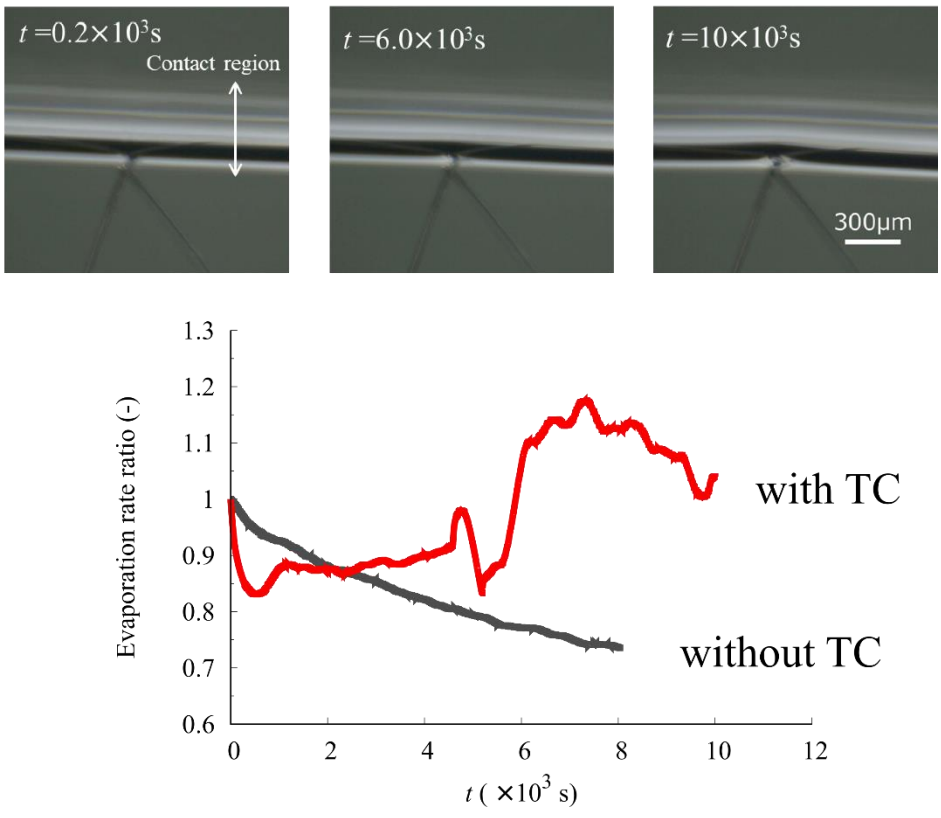

Fig. 3-10. (Top) Horizontal images showing deformed interface due to TC-tip
(Bottom) Temporal variations of evaporation rate

3.3.2 Results of experiments in 3.2.2

3 experiments were conducted with 3 different initial positions of the bottom of the meniscus: 10mm, 20mm, 30mm from channel exit. The maximum error is 2.7mm. Fig. 3-11 shows the receding distance as a function of time. It can be found that the data for 10mm and 5mm in channel size $2d$ have almost same gradient while the gradient tends to increase with reducing $2d$ less than 5mm. Because the gradient of data corresponds to apparent evaporation flux, the results show the dependence of apparent evaporation flux on channel size is significantly reduced for $d > \kappa_{cap}^{-1}$ because of the constant curvature. The experimental method and condition are totally different from the above experiments, but the change in the size-dependence around $d = \kappa_{cap}^{-1}$ is consistent.

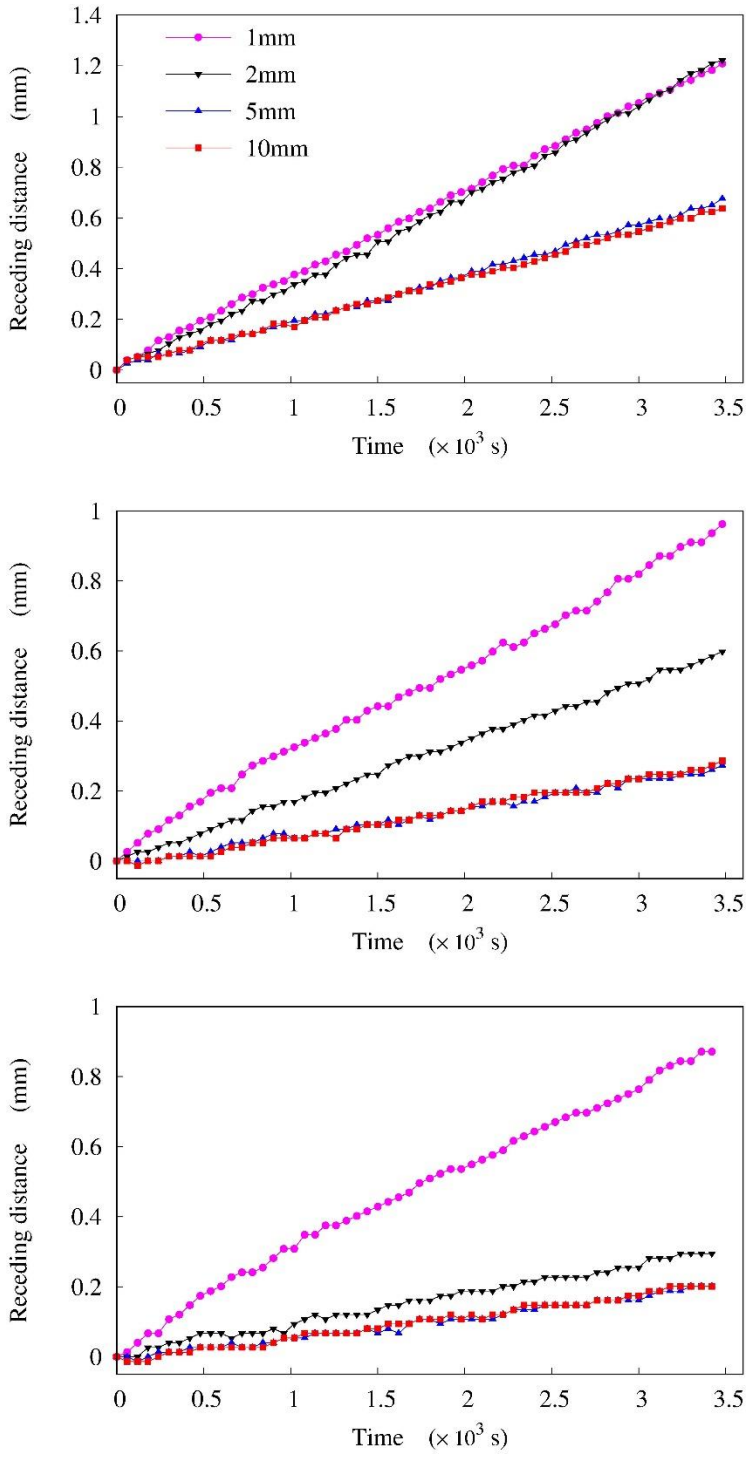

Fig. 3-11. Receding distance of menisci with initial position of (a) 10mm (b) 20mm (c) 30mm apart from channel exit. Legends in the top left in figure (a) shows channel size $2d$

3.4 Summary

The evaporation rates in various geometrical gap configurations made of glass were experimentally measured to know the dependence of evaporation flux in the condition of $d > \kappa_{cap}^{-1}$. The apparent evaporation flux was found to weakly depend on the inner perimeter of the channel for $d > \kappa_{cap}^{-1}$. Once the capillary lengths interfered to be $d \le \kappa_{cap}^{-1}$, the area-averaged evaporation flux was found to depend only on the meniscus curvature and increased with an increase in the curvature, which is confirmed in the previous chapter. In addition, the separate experiments were conducted to know the apparent contact angles and temperature of evaporating meniscus. The apparent contact angles measured by the laser interferometry kept constant within the experimental period. The temperature measuring by a miniature thermocouple demonstrates the evaporating cooling in the presence of the vapor diffusion layer. Interestingly, it was found that the evaporation rate significantly alters due to the deforming meniscus by a TC-tip, which is believed as the curvature effect.

Chapter 4 Scaling law for evaporation rates

4.1 Introduction

The previous chapter shows the evaporation flux strongly depends on the channel size in the condition of $d \le \kappa_{cap}^{-1}$, while the dependence for $d > \kappa_{cap}^{-1}$ is insignificant. The strong dependence of the evaporation flux in the narrow channel may be due to the interface curvature. Interestingly, it was reported by Sáenz et al [53] that the diffusion-limited evaporation rate from sessile-droplet whose size was smaller than κ_{cap}^{-1} is a function of area-averaged interface curvature. In the report, the scaling law for the evaporation rates with various geometrical shapes was proposed by the curve fitting as

$$\dot{m} = 2.24\left(c_i - c_\infty\right)\frac{D}{\bar{\kappa}}S^{0.53}, \tag{4.1}$$

where $c_i - c_\infty$ is the difference between the interface and far-field vapor concentrations, D is mutual diffusivity of air-vapor system, $\bar{\kappa}$ is area-averaged interface curvature and $S = A_i\bar{\kappa}^2$ is a dimensionless shape factor (A_i is interface area). This empirical correlation can be used for predicting the diffusion-limited evaporation rate from sessile droplets. It must be noted that the researchers in that study [53] argued strong evaporation at the 3-phase contact line due to the concentration gradient. Their discussion is based on the well-known diffusion problem [54–56], where the concentration gradient at the contact line exhibits significant, or sometimes infinite, due to the abrupt change in the boundary condition. This model is fundamentally different from thermal models mentioned in the Introduction, while both lead similar results that local evaporation maximizes at 3-phase contact-line.

In the case of the meniscus evaporation, there is no modeling work directly discussing on relating the evaporation kinetics and its shape. If the dependence of evaporation rates on interface shape is clarified, it would be helpful to physically investigate why the narrow channel exhibits strong evaporation. This chapter describes a model to mathematically show the dependence of the evaporation rate on the interface curvature. The diffusion model is macroscopic and the thin liquid film at the contact line is not considered. Finally, the author discusses the comparison between the derived scaling law for evaporation rate and experimental data.

4.2 Model

Consider the condition of $d \le \kappa_{cap}^{-1}$ to assume the meniscus shape as a spherical or cylindrical one as shown in Fig. 4-1. The diffusion-limited evaporation rate $\dot{m} = \int_{A_i} D\nabla_r c(\mathbf{r_i}) dA$ can be analytically rearranged in a simple manner, here, D is mutual diffusivity of air-vapor system, $c(\mathbf{r_i})$ is local vapor concentration at the interface location $\mathbf{r_i}$, ∇_r denotes differential operator in the radial direction. In the cylindrical coordinate system: $\mathbf{r_i} = (\kappa^{-1}, \varphi_i, z_i)$, where $0 \le \varphi_i \le \pi - 2\theta$ and $0 \le z_i \le w$, the evaporation rate can be expressed as

$$\dot{m} = \int_{A_i} D\nabla_r c(\mathbf{r_i}) dA = \int_{w_i}\int_{\varphi_i} D\nabla_r c(\mathbf{r_i}) \kappa^{-1} d\varphi dz \,. \tag{4.2}$$

By introducing an area-averaged concentration at the interface $c_i = \int_{A_i} c(\mathbf{r_i}) dA \Big/ \int_{A_i} dA$ and a far-field concentration c_∞ as a constant, the following simple relation can be derived

$$\dot{m} = fD(c_i - c_\infty)\kappa^{-1} S \,. \tag{4.3}$$

Here, $S = A_i \kappa^2$ is a dimensionless parameter representing for the meniscus interface shape and f is termed as evaporation factor in this study. Eq. (4.3) represents the evaporation rate linearly increases with the curvature and the interface area if the unknown evaporation factor does not depend on these shape parameters. Here, the analytical expression for the evaporation factor is

$$f = \frac{\int_{\varphi_i} \left(\dfrac{\partial c}{\partial r} \right)_{\mathbf{r}=\mathbf{r_i}} \kappa^{-1} d\varphi}{\int_{\varphi_i} \{ c(\mathbf{r_i}) - c_\infty \} d\varphi} \,. \tag{4.4}$$

To find the simple expression of the evaporation factor, the concentration is assumed to be linear between the interface $\mathbf{r_i}$ and the center of curvature $\mathbf{r_0} = (0, \varphi_i, z_i)$ as follows.

$$c(\mathbf{r_0}) = c(\mathbf{r_i}) - \kappa^{-1} \left(\frac{\partial c}{\partial r} \right)_{\mathbf{r}=\mathbf{r_i}} \,. \tag{4.5}$$

Here, the concentration variation along the interface is assumed to be negligible. Finally, the evaporation factor can be expressed as

$$f = \frac{\int_{\varphi_i} \{c(\mathbf{r}_i) - c(\mathbf{r}_o)\} d\varphi}{\int_{\varphi_i} \{c(\mathbf{r_i}) - c_\infty\} d\varphi} . \tag{4.6}$$

Because the boundary value problem was not defined in this model, the evaporation factor is still unknown, however, its maximum can be predicted as $f \approx 1$ when $c(\mathbf{r_o}) \approx c_\infty$. By substituting $f = 1$ to Eq. (4.3), the maximum evaporation rate is expressed as

$$\frac{\dot{m}\kappa}{D(c_i - c_\infty)} = S , \tag{4.7}$$

which is a similar form with Eq. (4.1) to relate the meniscus evaporation rate to the interface shape.

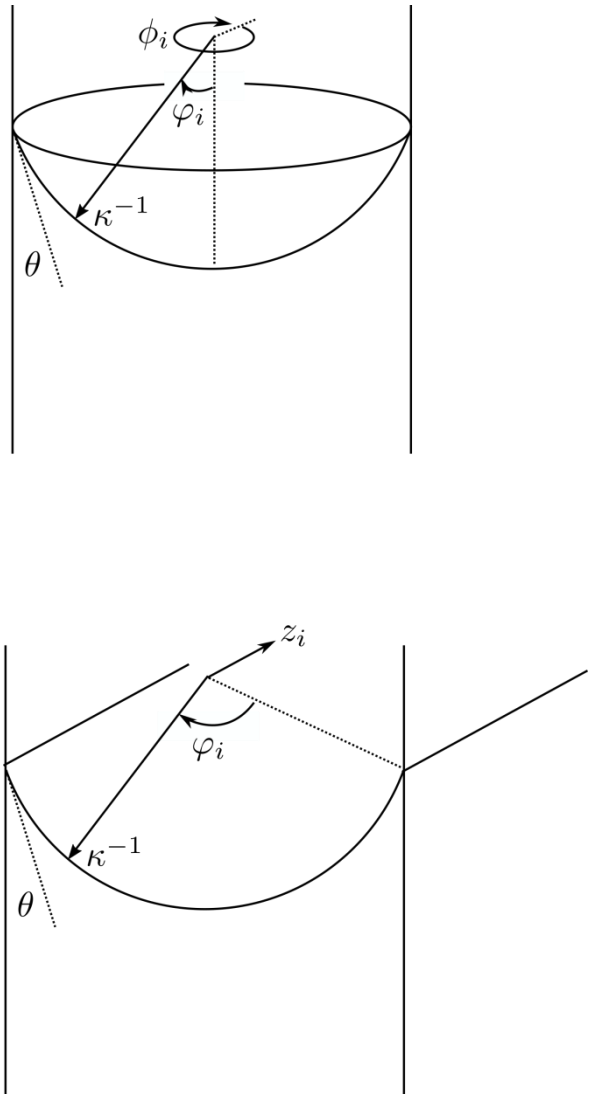

Fig. 4-1. Idealized spherical (top) and cylindrical (bottom) meniscus shape.

4.3 Application to present and previous data

First, the experimental data presented in Section 3.3.1 was compared with the proposed scaling law for the evaporation rate. The mutual diffusivity D of the air-vapor system was theoretically evaluated [57] with the temperature and pressure in the enclosure. By making use of the difference of the partial pressure, $c_i - c_\infty$ was approximated as $(1-0.78)c_{sat}$ in that experiment. Here, c_{sat} is a saturation concentration of vapor. In Fig. 4-2, the maximum values of the evaporation rates for each shape factor experimentally obtained were compared with Eq. (4.7), except for the petri-dish cases because A_1 and κ were unknown. The experimental data is consistent with Eq. (4.7) which shows the linear relation in the dimensionless evaporation rate and S. In the experiments, the evaporation rate decreased as time progressed because the vapor pressure in the system gradually approached the saturation value. This tendency is consistent with Eq. (4.6) which shows the evaporation factor decreases as $c(\mathbf{r_0})$ approaches the saturation concentration.

Basically, the scaling law should be applicable to evaporation of any type of liquid in any simple interface configuration if the process is diffusion-limited. Hence, the author next compared the scaling law with the experimental data for the volatile liquids in the capillaries ($d = 0.10 \sim 0.45$ mm) reported by Buffone [42]. Fig. 4-3 shows the maximum evaporation rates of the 4-type volatile liquid in the capillaries predicted by Eq. (4.7). The horizontal axis is measured value in reference [42]. Fig. 4-3 is intended to show the relation between the predicted maximum rates and the experimental data. The latter is expected to be linear with and less than the former, if Eq. (4.3) with $f = 1$ is correct. To do that, several assumptions were made for the experimental data [42]. The first assumption is $\cos\theta \approx 1$. This assumption could not be irrelevant by considering the careful preparation for the glass tubes and low surface energies of the working fluid. Secondary, it was assumed that the test section is isothermal at room temperature. This assumption leads to overestimating the saturation concentration. For example, the 10K decrease leads to 30% decrease in the saturation pressure for Pentane [58]. This change may not be trivial for discussing the linearity for high evaporation cases, but it can also be found that the predicted maximum rates still larger than the measured values. The last assumption is c_∞, far-field concentration, equals zero. In that experimental condition [42], where the volatile liquid evaporated into the atmosphere, it is natural to consider c_∞ is much smaller than the saturation concentration. Hence, this assumption could also not bad. In conclusion, Eq. (4.3) with $f = 1$ maybe correct according to Fig. 4-3, although several assumptions must be made and more experimental data would be necessary for more accurate comparison.

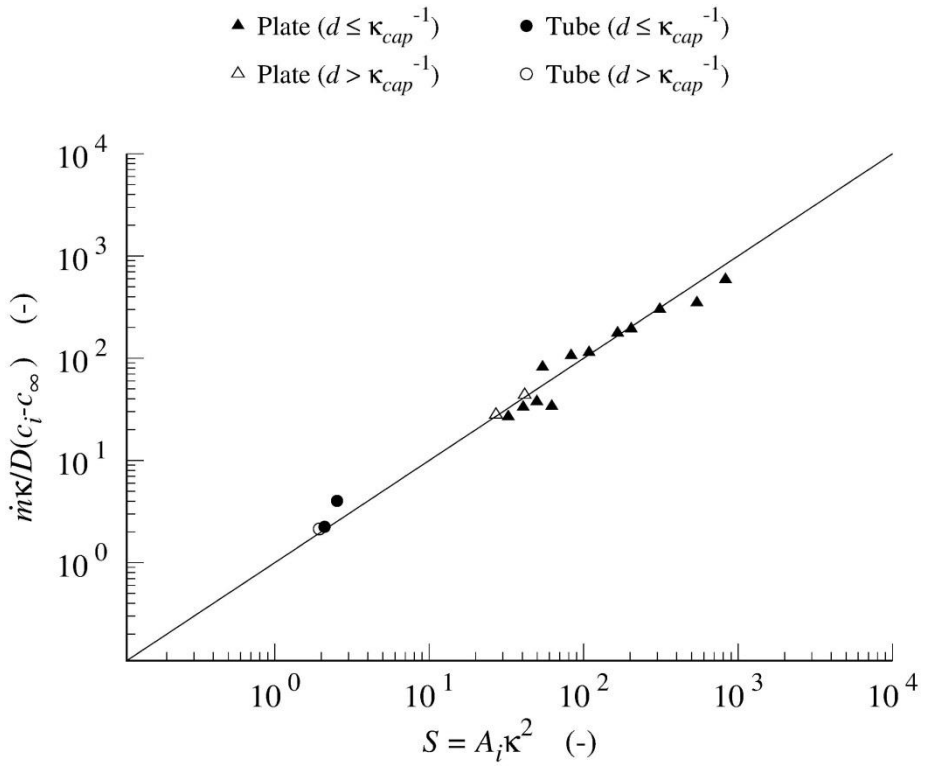

Fig. 4-2. Comparison with experimental data and scaling law. Solid line shows Eq. (4.7).

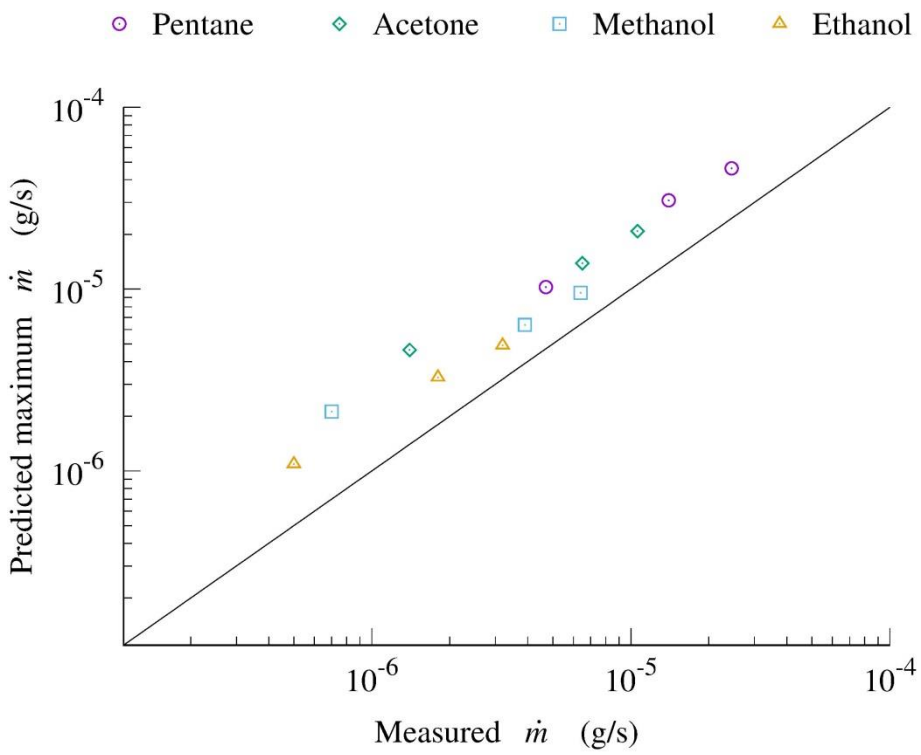

Fig. 4-3. Evaporation rates in capillary tubes [42] and maximum values predicted by Eq. (4.3) with $f = 1$.

4.4 Summary

The scaling law to relate the evaporation rates to the various interface shape of the interfered menisci was derived from the macroscopic model. By using the maximum evaporation factor, the scaling law can predict the maximum evaporation rate and the good agreement is shown with the experimental data presented in Section 3.3.1. In addition, the applicability of the scaling law to volatile organic liquid in capillaries was discussed. The author confirmed the qualitative agreement, although several assumptions must be made and more experimental data would be necessary for more accurate comparison.

Chapter 5 Mechanisms for evaporation enhancing effect

5.1 Introduction

As discussed in the Introduction, the evaporation enhancing effect has been attributed to 2 possible physics in previous studies; one is the strong evaporation flux in the thin-film region for pure vapor condition and another is an increase in interface area due to nanoscopic precursor film for nanochannel. In the case of a macroscopic evaporating meniscus in the presence of the diffusion layer, however, the thermal resistance of the liquid film is negligibly small and the additional evaporating area due to the precursor nanofilm may not be significant compared to the intrinsic meniscus [36]. Therefore, the author postulated that there exists a certain evaporation source at the gas/liquid interface and it depends on channel size. In other words, the evaporation enhancing effect may be attributed to the potential difference, not the resistance of liquid film nor additional evaporating area. This means that an additional vapor pressure term should be considered at the interface. Indeed, in the conventional thermal models, the excess term has been used to show the deviation from the equilibrium. For example, Moosman & Homsy [15] clearly described an additional pressure term in the interface mechanical balance, which acts as a source term in an expression of the evaporation flux. The other models (such as [16]) also treated it implicitly as the pressure difference across the gas/liquid interface. In these models, however, the term is treated as the stress field associated with flow caused by evaporation and local thermodynamic equilibrium at the interface is assumed, which leads to a given potential difference. In the present chapter, the author changes the interpretation of the term and demonstrate how the excess pressure term without local thermodynamic equilibrium in the micro region leads to the size-dependent evaporation flux by a modeling work.

The proposed model describes local evaporation characteristics in the micro region of a stationary meniscus between hydrophilic vertical parallel plates. Prior to the description of the overall mass transfer equation, the author clarified a length scale to be focused on in the multiscale structure of the liquid film. Since some assumptions of previous models did not hold for a binary system, a minimum free-energy technique was used. The author derived the equation describing the overall mass transfer with some simplifications which are applicable near the contact line and then analyzed the experimental data for the diffusion-controlled evaporation process. In the present model, heat conduction in the liquid film and kinetic effects were also considered in addition to vapor diffusion to clarify how the result based on the conventional thermal models

changes in the presence of the diffusion layer. Although the evaporation resistance due to kinetics could be practically small in the investigated condition, it was considered because the thickness of the Knudsen layer is comparable with the microscopic length scale the model focuses on.

5.2 Model

Consider a two-dimensional meniscus formed between parallel plates immersed in a pool filled with liquid, as shown in Fig. 5-1. A vertical distance from pool to contact line is h and a horizontal channel distance is $2d$, where d is smaller than the capillary length and much larger than an adsorbed film thickness δ_e. ℓ is the distance from contact line to channel exit. Let ℓ be a diffusion length scale used in diffusive vapor transfer. An apparent contact angle θ is much smaller than unity and the film thickness u depends only on a coordinate x as $y = u(x)$, where *x*-axis lies in a plane at the surface of solid facing the liquid phase; the coordinate origin is defined at the contact line. The system consists of an evaporating liquid component and an inert and non-condensable gas. This analysis needs 5 boundary conditions in the confined space: a surface of solid facing liquid phase; a gas/liquid interface at liquid side (BC-3); a gas/liquid interface at gas side (BC-2); a boundary between Knudsen layer where heat & mass transfer is kinetically controlled and a continuum region where equations of continuum fluid mechanics can apply (BC-1); a channel exit (BC-0). The surface temperature of the solid wall is set to constant and denoted as T_w^*. BC-1 is located at about one mean-free-path of vapor molecule away from the gas/liquid interface. For simplicity, physical quantities at each boundary (BC-0 ~ BC-3) are denoted as $[*]_{0\sim3}$. At equilibrium, this system is isothermal and the partial pressure of vapor p_v and total pressure p are constant. Hereafter let consider that this equilibrium is broken by reducing $[p_v]_0$ with $[T^*]_0 = T_w^*$. This model includes heat conduction in liquid film because evaporation driven by the partial pressure consumes the heat transferred from ambient, even if there was no artificial heating.

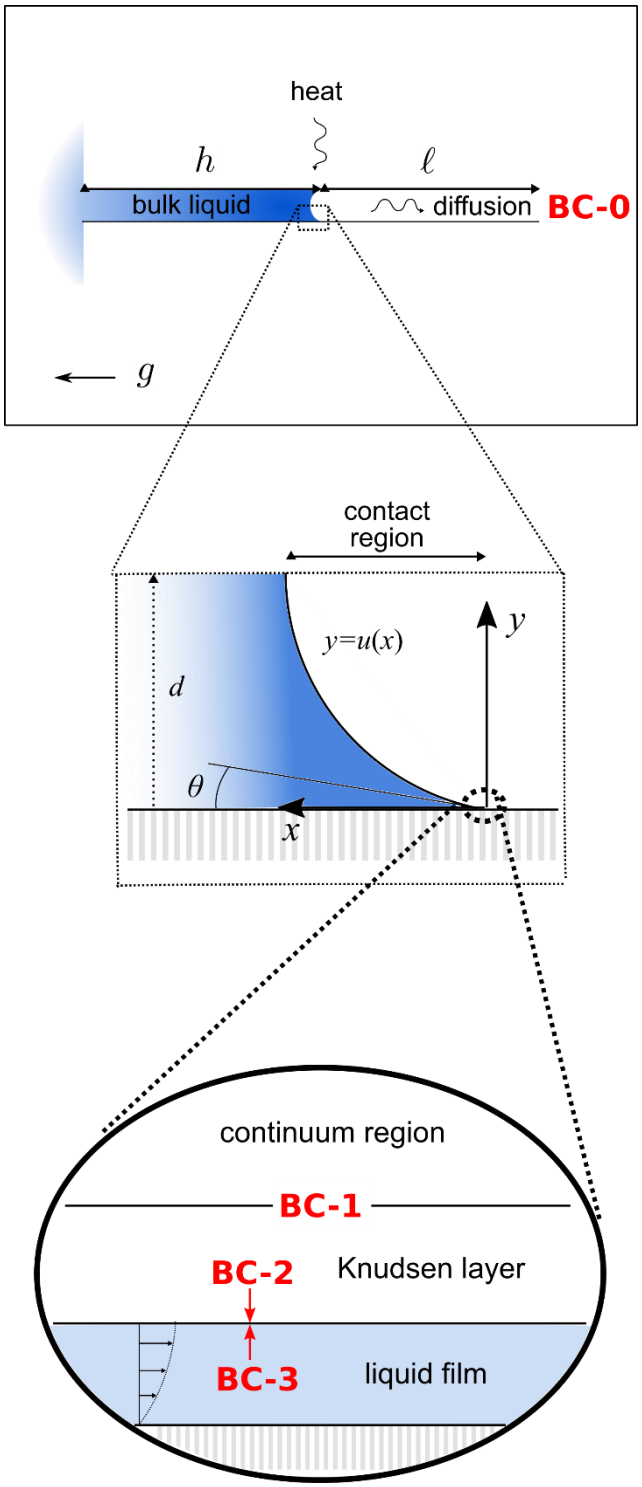

Fig. 5-1. A conceptual drawing of a meniscus between hydrophilic solid surfaces with adsorbed films.

5.3 Microscopic structure

If a single component system is considered, the well-known model [21] for the multiscale problem is applicable. However, as a binary system is considered in this study, several basic equations (e.g. Eqs. (2)-(7) in the reference) regarding thermodynamics and mechanical equilibrium for the single-component system do not hold. Hence, the author took a different approach to describe the microscopic structure. To describe the shape of the liquid film whose thickness is less than micro-scale (typically 1μm), certain intermolecular forces must be considered, such as universally existing dispersion forces, or electrical double layer's forces for an ionic solution. Disjoining pressure $\Pi(u)$ is related to the excess potential energy acting on a planar film per unit area $P(u)$ via $\Pi(u) = -dP(u)/du$. For $u'^2 = (du/dx)^2 \ll 1$, the decomposition of the free energy F proposed by de Gennes [22] is given by

$$F = F_0 + \int_0^d dx \left\{ \frac{\sigma}{2}\left(\frac{du}{dx}\right)^2 + P(u) + G(u) \right\}. \tag{5.1}$$

The homogeneous term F_0 in Eq. (5.1) is treated as a constant. The second term is an inhomogeneous part and the interval of integration corresponds to the contact region. The first term in large brackets denotes a surface excess energy in gas/liquid interface (σ is surface tension) and the last term $G(u)$ is a gravitational effect. The minimization of Eq. (5.1) with respect to $u(x)$ gives a mechanical equilibrium condition for $x \ll h$ as follows:

$$\sigma \frac{d^2u}{dx^2} + \Pi(u) = \frac{dG(u)}{du} = \rho g h. \tag{5.2}$$

ρ is liquid density, and g is gravitational acceleration. The last important equation to describe an equilibrium liquid-film shape is given by multiplying u' and rearranging Eq. (5.2) as,

$$\frac{d}{dx}\left\{ -\frac{\sigma}{2}\left(\frac{du}{dx}\right)^2 + P(u) + G(u) \right\} = 0. \tag{5.3}$$

The liquid film shape can be calculated by giving a disjoining pressure $\Pi(u)$. Here, the well-known expressions for $\Pi(u)$ and $P(u)$ are introduced:

$$\Pi(u) = \frac{A_d}{u^3}, \qquad P(u) = \frac{A_d}{2u^2} = \frac{\sigma a_m^2}{2u^2}, \tag{5.4}$$

where non-retarded Hamaker constant is $-6\pi A_d$ and $a_m = \sqrt{A_d/\sigma}$ is a constant called a molecular length scale (~ 1Å). In general, disjoining pressure is a sum of non-retarded and retarded dispersion forces and a double layer forces for ionic solution. However, such general expression is inconvenient to describe a model analytically, so only non-retarded Hamaker constant is considered.

Eq. (5.3) was solved by neglecting a gravitational effect to obtain liquid film shape in an isothermal region closest to the contact line. In concrete, substituting the potential of Eq. (5.4) into Eq. (5.3) and performing the indefinite integration with fixing $G(u)$, the following equation can be found;

$$\left(\frac{du}{dx}\right)^2 - \frac{a_m^2}{u^2} = \Theta^2. \tag{5.5}$$

The interfacial gradient approaches a constant Θ with thickening liquid film. By integrating Eq. (5.5), a hyperbolic shape of $y = u(x)$ was obtained, which had an asymptotic form of $u = \Theta x$ as $x \to \infty$. Because an assumption of $u'^2 \ll 1$ cannot be applied near the crossing point between the hyperbola and *x*-axis, it is necessary to consider a connection between the adsorbed film whose thickness is δ_e and the region whose growth is characterized by Θ. To solve this problem, the author considered a mechanical equilibrium condition for which these regions coexisted. From this viewpoint, the grey portion in Fig. 5-2 should be filled with liquid. By matching the two solutions, the interfacial gradient at the micro region adjacent to the contact line, or a microscopic contact angle, can be described by a relation of $\Theta \sim a_m/\delta_e$. This linear region named Ia. The point between Ia and the adsorbed film should be connected smoothly by the molecular behavior. Here, the thickness of the adsorbed film, δ_e, satisfies the following equation:

$$\delta_e = \sqrt[3]{\frac{a_m^2 \varepsilon d}{\cos\theta}} \approx \sqrt[3]{a_m^2 \varepsilon d}. \tag{5.6}$$

Eq. (5.6) includes ε corresponding to a dimensionless curvature in the previous theory [16]

whose range is 0 to 1.

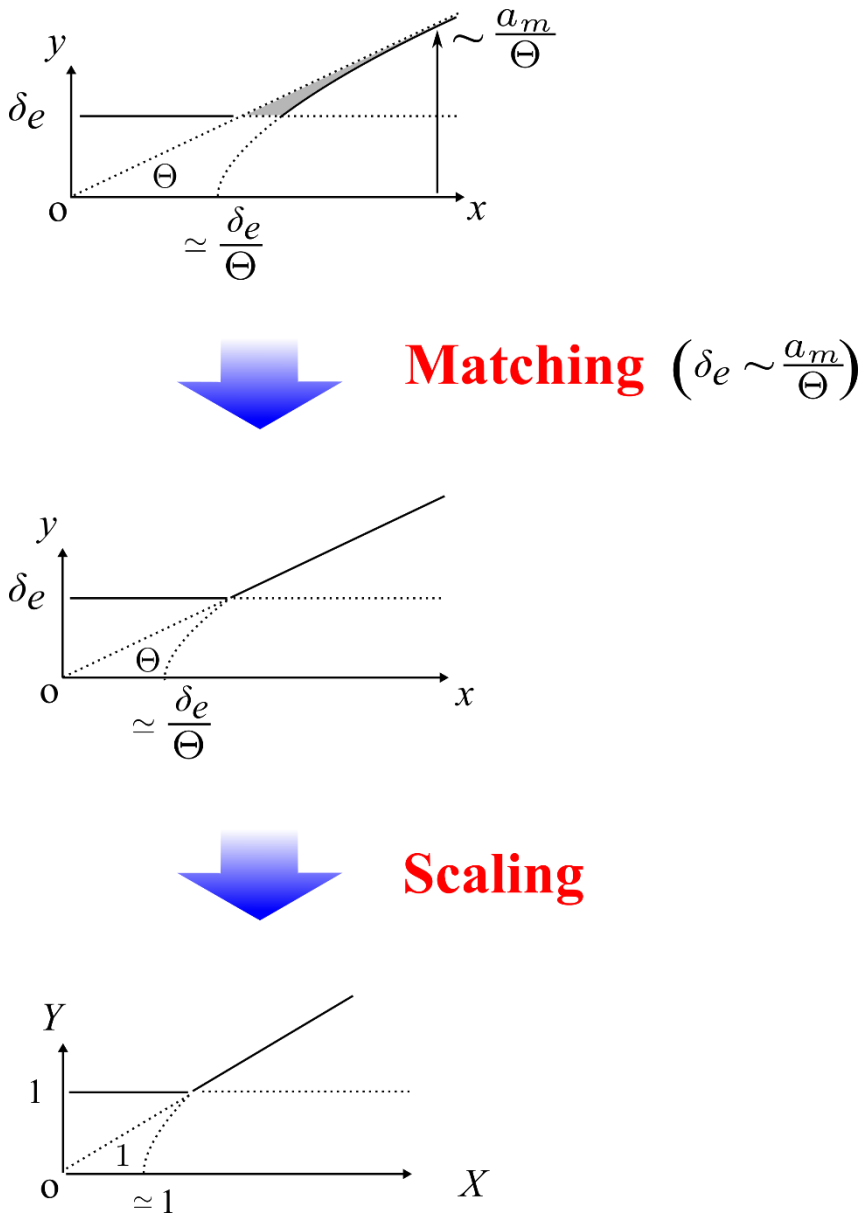

Fig. 5-2. Matching condition between adsorbed film and micro region, and its scaling.

In micro region, liquid film can evaporate if the attractive intermolecular forces weaken. The mechanical equilibrium of Eq. (5.2) alters in non-isothermal case. In the liquid side, there is an upward flow to feed liquid to the meniscus. On the other hand, evaporation causes a temperature gradient near the contact line and thus induces the Marangoni stress. In this analysis, the surface tension was treated as a constant, which gave the upper limit of evaporation flux. The flow fed into the liquid film takes part in interface distortion, but the interpretation in the present model is different from the previous theories [15]. Assuming the gas phase on gas/liquid interface (BC-2) can have an excess vapor pressure relative to the liquid-phase pressure (BC-3), the mechanical equilibrium condition at the interface can be described as follows:

$$\begin{aligned} \rho g h &= [p]_2 - [p]_3 \\ &= [p_{eq}]_2 - [p]_3 + p_{ex} \\ &= \sigma \frac{d^2 u}{dx^2} + \Pi(u) + p_{ex}. \end{aligned} \tag{5.7}$$

The first equality of Eq. (5.7) is appropriate if $x \ll h$ and the total pressure is constant. The second equality shows explicitly a deviation from equilibrium by using an additional phenomenological pressure term p_{ex}. If there is evaporation, p_{ex} is greater than zero and acts as a source for evaporation. This excess pressure must be identical to normal stress due to the flow fed into the liquid film to maintain a stationary meniscus, therefore the above equation is the same in form as a conventional stress balance. By defining a dimensionless liquid film thickness and *x*-coordinate,

$$X = \frac{x}{\delta_e / \Theta}, \quad U = \frac{u}{\delta_e}, \tag{5.8}$$

and setting the boundary conditions at the contact line as $U = 1$, $U' = 0$ and $U'' = 0$, the pressure balance can be expressed as follows:

$$1 - \frac{p_{ex}}{p_d} = \frac{d^2 U}{dX^2} + \frac{1}{U^3}, \tag{5.9a}$$

$$\frac{p_{ex}}{p_d} \to 0 \quad \text{as} \quad X \to 0, \tag{5.9b}$$

$$\frac{p_{ex}}{p_d} \to 1 - \varepsilon, \quad \text{where} \quad \varepsilon = \frac{\sigma \cos\theta / d}{p_d} \quad \text{as} \quad X \to \infty. \tag{5.9c}$$

p_d is disjoining pressure at the contact line. Eq. (5.9b) shows the condition required at the adsorbed film. Equation (5.9c) is the boundary condition required for the macro region *II*, where the large-scale interfacial curvature is expressed as $\cos\theta/d$. ε is a ratio of macroscopic capillary pressure to disjoining pressure at the contact line. $\varepsilon = 1$ shows the equilibrium and $\varepsilon < 1$ shows that the liquid flow is caused by the difference between disjoining and capillary pressures.

It is known that, if the evaporation is controlled by liquid film conduction and kinetic mass transfer, a large local evaporation flux causes a local maximum of interface curvature in the micro region (see [11,12,59]). In this case, the mesoscopic length scale should be considered as Morris [19] discussed. However, this is the limiting case as mentioned later. The present model demonstrates that the local evaporation flux cannot be significant in the micro region and a local maximum of interface curvature does not appear if evaporation is controlled by diffusion. This means the interfacial curvature in the micro region monotonically goes from zero in the adsorbed region to a constant in the macro region [25]. Therefore, the present model focuses on the micro region characterized by the microscopic length scale of Eq.(5.8). Before describing heat and mass transfer for evaporation, the author attempts to demonstrate the validity of the discussion for the microscopic length scale by using a simple model for the wetting film profile in equilibrium.

5.4 Discussion on microsopic length scale

In this section, a simple model is proposed to describe the shape of liquid film on a hydrophilic plate consisting of the linear region Ia, the macro region II, and the mesoscopic transition region Ib. The connecting points are defined at X_1 for Ia and Ib, and at X_2 for Ib and II. To satisfy curvature continuity, a cubic polynomial was used to express the transition region. The zeroth, first and second derivatives for U at X_1 are known. At the far left of region II, an apparent contact angle must be defined as an interfacial gradient. To define an "apparent" interfacial gradient, an empirical parameter $\delta = 1\,\mu\text{m}$ is used, i.e., $U_{X=X_2} = \delta/\delta_e$. Introducing such the empirical parameter is open to discussion, as well as introducing the polynomial function, but these assumptions would not affect this model's objective to demonstrate the validity of the microscopic structure near the contact line. The first and second derivatives are then given by $U'_{X=X_2} = \theta/\Theta$ and $U''_{X=X_2} = \varepsilon$ from the boundary condition of Eq. (5.9c). Using these boundary conditions, each coefficient of a cubic function can be calculated analytically. Because there is a discontinuity at each boundary of Ia, the additional condition $X_1 \to \sqrt{2}$ was applied to the crossing point where Ia and adsorbed regions meet. Then, the interfacial curvature in the micro region goes linearly from zero in adsorbed region to a constant in the macro region II. The interface shape in the macro region is obtained by a circular arc smoothly connecting to Ib at X_2. The curvature of the arc is $d/\cos\theta$ for $d \gg \delta$ as tabulated in Table 5-1.

Table 5-1. Expressions for the subregions and several dimensionless quantities

Subregions:

$$U = X \quad \text{for} \quad Ia$$

$$U = f_1(X^3 + f_2X^2 + f_3X + f_4) \quad \text{for} \quad Ib \qquad \{f_{1\sim4} \text{ are functions of } \theta, \Theta, D_2, \alpha, \varepsilon\}$$

$$\left(\frac{X}{\Theta} + R_1\right)^2 + (Y - D_1)^2 = R_2^2 \quad \text{for} \quad II \qquad \left\{R_1 = \theta(D_1 - D_2) - \frac{X_2}{\Theta}, R_2 = (D_1 - D_2)\sqrt{\theta^2 + 1}\right\}$$

Dimensionless quantities:

$$X_1 = -\frac{f_2}{3} = \sqrt{2}, \qquad X_2 = \frac{\varepsilon - 2f_1f_2}{6f_1}, \qquad D_1 = \frac{d}{\delta_e},$$

$$\Theta = \alpha\frac{a}{\delta_e}, \qquad \theta = \frac{a}{\delta_e}\sqrt{-3 + \frac{1}{D_2^2} + 2D_2}, \quad D_2 = \frac{\delta}{\delta_e}$$

$$\alpha = 2\sqrt{-3 + \frac{1}{D_2^2} + 2D_2}\left\{-1 + \sqrt{9 + 6\varepsilon(D_2 - \sqrt{2})}\right\}^{-1}, \quad \delta_e \approx \sqrt[3]{a^2\varepsilon d}.$$

Given quantities: $a, d, \delta, \varepsilon$

A microscopic contact angle Θ can be related to macroscopic parameters by integrating Eq. (5.3) from adsorbed region to $X \to \infty$ in Ib including a gravitational effect. By using Eqs. (5.2), (5.8) and $\Theta = \alpha a / \delta_e$, where $\alpha = O(1)$ is a modification factor, the dimensionless form of Eq. (5.3) can be expressed as

$$\frac{d}{dX}\left\{-\left(\frac{dU}{dX}\right)^2 + \frac{1}{\alpha^2 U^2} + \frac{2U}{\alpha^2}\right\} = 0. \tag{5-10}$$

α is given by letting $X_1 = \sqrt{2}$. Integrating the above equation from 0 to X_2 and rearranging, the following relationship for the contact angles was obtained:

$$\frac{\theta}{\Theta} = \frac{1}{\alpha}\sqrt{-3 + \frac{\delta_e^2}{\delta^2} + \frac{2\delta}{\delta_e}}. \tag{5-11}$$

The discussion above is tabulated in Table 5-1. By using this approach, two experimental data were analyzed. Firstly, the author applied the model to the experimental data reported in [17,23]. It should be noted that the meniscus forms horizontally at the channel exit, not vertically in their study. The difference in meniscus orientation is trivial because hydrostatic pressure just changes to reservoir pressure maintained at a constant level [17]. By using the reported adsorbed film thickness and the material properties including Hamaker constants reported in [16], the shape of the micro region at isothermal condition was compared, as shown in Fig. 5-3. These graphs show a good agreement near the contact line and the discussion for Ia is appropriate. On the other hand, the present model shows poor agreement near macro-region in all cases. The discrepancies are not the same but depend on the working fluid. The maximum error of the apparent contact angle relative to the experimental data was 106%. It is considered this disagreement is based on the value of δ. As mentioned above, the author chose $\delta = 1$ μm empirically, not theoretically. It should depend on the strength of disjoining and capillary pressures, by considering the definition of δ, that is, the boundary between the micro and macro regions. Hence, it is not surprising that δ is different for different kinds of the working fluid. In addition, δ should depend on d, which is obvious for $d \to \delta_e$. The analytical expression of δ is difficult to derive and it needs further investigations.

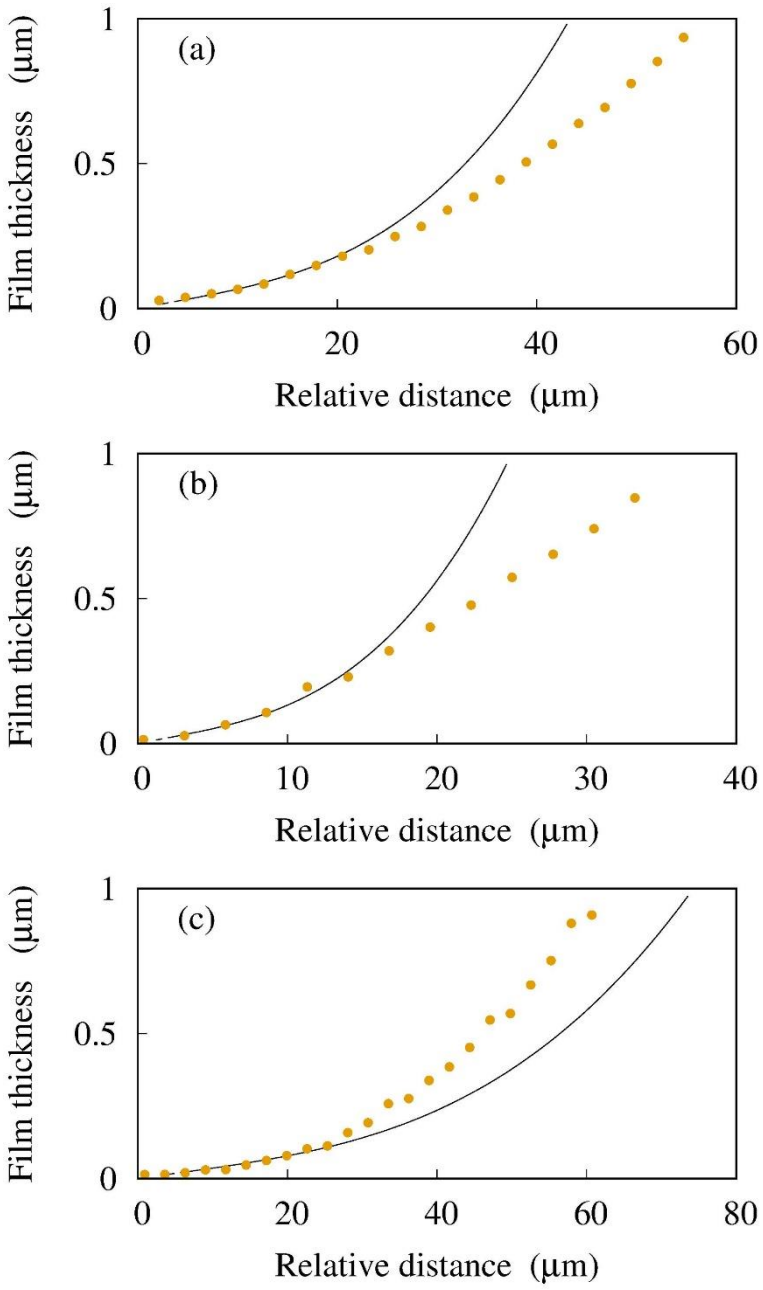

Fig. 5-3. Application to experimental data reported in [17,23] for (a) heptane, (b) R113 and (c) propanol. Solid line shows model output and dots show the experimental data. Material properties including Hamaker constants were presented in [16]

Next, the model was applied to the evaporation experiments presented in Section 3.3.1 just for reference. In the experiments, the meniscus formed in a narrow channel of $2d$ in width between parallel glass plates vertically immersed in a water pool. The input parameters are listed in Table 5-2. Hamaker constant at room temperature was obtained by the simplified Lifshitz theory [52]. The calculated results are listed in Table 5-2 and the resulting shape is shown in Fig. 5-4. It is found that the predicted apparent contact angle (7.0×10^{-2}) is a few times larger than the experimental value (1.55×10^{-2}) for $\delta=1$ μm, though both values are the same order of magnitude. In addition to the problem on δ, it may be caused by another reason: the adsorbed film in the experiment is thicker than that obtained by the present model. It is probable if additional disjoining pressure is caused by the electric double-layer force which acts to thicken the adsorbed film for the purified water on the glass [22,52].

In conclusion, although this analysis for describing the equilibrium shapes of the micro region needs to be further improved in some respects, the predicted micro contact angles show good agreements with the experimental data, which demonstrates the validity of the discussion for the microscopic length scale.

Table 5-2. Application to experimental data for water presented in Section 3.3.1: list of input and output parameters

input	A_d	8.1×10^{-22}	(J)
	σ	69.2×10^{-3}	(N/m)
	a	1.1×10^{-10}	(m)
	d	0.40×10^{-3}	(m)
	δ	10^{-6}	(m)
	ε	1	(–)
output	δ_e	1.7×10^{-8}	(m)
	D_2	60	(–)
	D_1	2.4×10^{4}	(–)
	α	1.2	(–)
	θ	7.0×10^{-2}	(–)
	Θ	7.8×10^{-3}	(–)

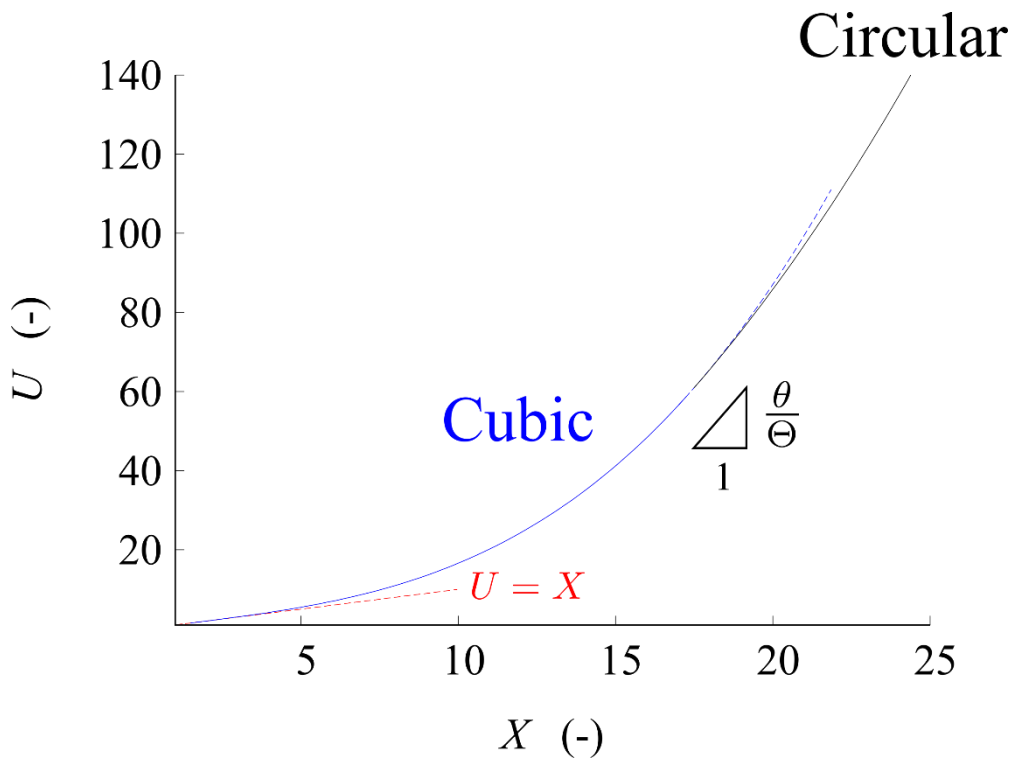

Fig. 5-4. Application to experimental data for water presented in Section 3.3.1: dimensionless film shape consisting of linear, cubic and circular subregions.

5.5 Heat and mass transfer

To describe static evaporation characteristics in the micro region consisting of Ia and Ib, the model considers the liquid film conduction, kinetic mass transfer, and diffusion without the assumption of local thermodynamic equilibrium in the micro region. At first, several scales and non-dimensional quantities were defined as follows;

$$\begin{aligned} p' &= \frac{\rho \upsilon v'}{\delta_e \Theta}, \quad \Delta T^* = T_w^* - T_{sat}^*\left([p_v]_0\right), \quad Re_m = \frac{v'\delta_e}{\upsilon}, \\ P &= \frac{p}{p'}, \qquad T = \frac{T^* - T_{sat}^*\left([p_v]_0\right)}{\Delta T^*}, \qquad J = \frac{j}{\rho v'}. \end{aligned} \tag{5.12}$$

v', υ and j are characteristic velocity, kinetic viscosity, and evaporation flux, respectively. The characteristic velocity v' is undetermined at this point. Because δ_e is very small, Re_m is much smaller than 1. The mass and momentum conservation laws in liquid phase with non-slip condition on the solid surface and free slip condition at gas/liquid interface yields

$$J = \frac{d}{dX}\left(\frac{U^3}{3}\frac{d[P]_3}{dX}\right). \tag{5.13}$$

The well-known expression for kinetics [21] is based on a change of thermodynamic quantities of liquid and vapor, and some basic equations in equilibrium do not hold in this system. Hence, Schrage's equation [60] was used for the rate of vapor transfer from BC-2 to BC-1:

$$j = H\left(\frac{[p_v]_2}{\sqrt{2\pi R_v [T^*]_2}} - \frac{[p_v]_1}{\sqrt{2\pi R_v [T^*]_1}}\right), \tag{5.14}$$

where H and R_v are Schrage's accommodation factor and specific gas constant of vapor, respectively. Strictly speaking, an inappropriateness of Schrage's equation was pointed out in [61], and it is limited to use as $1 > [T^*]_1/[T^*]_2 > \left([p_v]_1/[p_v]_2\right)^2$. Under these limitations, Schrage's equation can be used qualitatively. Since the original form of Schrage's equation was inconvenient to describe the connection at these boundaries, the author used a linearized form [62] around BC-0 as follows:

$$j = c_1([p_v]_2 - [p_v]_1) - c_2([T^*]_2 - [T^*]_1), \tag{5.15}$$

$$\text{where} \quad c_1 = \frac{H}{\sqrt{2\pi R_v [T^*]_0}}, \quad c_2 = \frac{H[p_v]_0}{2[T^*]_0\sqrt{2\pi R_v [T^*]_0}}.$$

The coefficients were given by the first-order approximation. This equation gives an evaporation resistance due to kinetics at the interface, which becomes significant as the accommodation factor decreases and acts to suppress the strong evaporation in the micro region.

The energy consumed by evaporation transferred in one-dimensional heat conduction, which is appropriate if $\Theta \ll 1$ and $Re_m \ll 1$, then

$$j = \frac{c_1([p_v]_2 - [p_v]_1) - c_2(T_w^* - [T^*]_1)}{1 - h_{fg} c_2 u/\lambda}. \tag{5.16}$$

λ and h_{fg} are thermal conductivity of liquid and latent heat of evaporation, respectively. Eq. (5.16) can be expressed as the following dimensionless form by using $T_w^* - [T^*]_1 \approx \Delta T^*$,

$$\rho v' J = c_2 \Delta T^* \frac{c_4([P_v]_2 - [P_v]_1) - 1}{1 - c_3 U}, \tag{5.17}$$

$$\text{where} \quad c_3 = \frac{h_{fg} c_2 \delta_e}{\lambda}, \quad c_4 = \frac{c_1 \upsilon}{\delta_e \Theta}.$$

The characteristic velocity v' is chosen to satisfy $\rho v' = c_2 \Delta T^*$.

The rate of vapor transfer from BC-1 to BC-0 is given by

$$J = k c_5([P_v]_1 - [P_v]_0), \quad \text{where} \quad k = \frac{D}{\ell}, \quad c_5 = \frac{p'}{c_2 \Delta T^* R_v [T^*]_0}. \tag{5.18}$$

D and ℓ are diffusion coefficient and diffusion length scale, respectively. $[P_v]_1$ in the micro region is assumed to be independent of the macro region. In practice, a dense vapor layer exists above the macro region and $[P_v]_1$ in the micro region should be comparable to that in the macro region. Hence, this assumption gives the overestimated results for the micro region, as well as the assumption for thermo-capillary flow. In addition, the diffusion length scale was assumed to be much longer than the microscopic length scale, hence the diffusion length scale is independent on

the position. Substituting Eq. (5.18) into Eq. (5.17) for eliminating the pressure at BC-1, the author obtained an equation in which all resistances in liquid and gas phases are considered. For the static evaporation, the local evaporation flux must be identical to the loss of the volumetric rate of Eq. (5.11).

The innovative point in the present model is to introduce an excess pressure balancing with the stress field, which means a local thermodynamic equilibrium is not assumed. The following flux balance equation in the micro region is obtained by letting $P_{ex} = [P]_2 - [P_{eq}]_2 = \beta([P_v]_2 - [P_{v,eq}]_2)$ with an empirical factor β $(0 < \beta \ll 1)$ to show the presence of inert gas,

$$\frac{d}{dX}\left(\frac{U^3}{3}\frac{d[P]_3}{dX}\right) = R\left(\frac{P_{ex}}{\beta} - c_4^{-1} + [P_{v,eq}]_2 - [P_v]_0\right), \tag{5.19}$$

where R is reciprocal overall resistance for heat and mass transfer, namely, thin liquid film conduction, evaporation, and diffusion. The physical meaning of β is equality of total pressure. The model admitted the existence of excess vapor pressure at the interface, but uniform total pressure in the gas phase is preferable. This is achieved by $\beta \to 0$. The third term in the brackets of the right-hand side of Eq. (5.19) means the vapor pressure at which vapor and liquid can coexist, i.e., the saturation pressure of vapor at $[T]_3$;

$$[P_{v,eq}]_2 = P_{sat,T=[T]_3}, \quad \text{where} \quad [T]_3 = 1 - c_3 UJ. \tag{5.20}$$

Since a reciprocal overall resistance R is a function of liquid film thickness to express a thin liquid film thermal resistance, the mass flux balance is a nonlinear differential equation as follows;

$$J = \frac{1}{(kc_5)^{-1} + c_4^{-1}(1 - c_3 U)}\left(\frac{P_{ex}}{\beta} - c_4^{-1} + P_{sat,T=[T]_3} - [P_v]_0\right). \tag{5.21}$$

Expanding the saturation pressure until the first order gives,

$$P_{sat,T=[T]_3} \approx P_{sat,T=1} - \frac{dP_{sat,T=1}}{dT} c_3 UJ. \tag{5.22}$$

By substituting this saturation pressure into Eq. (5.21), the overall resistance R^{-1} is expressed as,

$$R^{-1} = (kc_5)^{-1}\left\{1 + kc_5c_4^{-1} + \left(c_4\frac{dP_{sat,T=1}}{dT} - 1\right)kc_5c_4^{-1}c_3U\right\}. \tag{5.23}$$

This equation can be rearranged and simplified by using Clausius-Clapeyron relation and considering $[T]_0 = 1$ and $\rho_{v,sat}h_{fg}/p_{sat} \sim 10$, namely,

$$R^{-1} \approx (kc_5)^{-1}\left(1 + \underbrace{\frac{k}{H}\sqrt{\frac{2\pi}{R_vT_w^*}}}_{\text{E/D}} + \underbrace{k\frac{\rho_{v,sat}^2h_{fg}^2}{p_{sat}\lambda T_w^*}\delta_eU}_{\text{T/D}}\right), \tag{5.24}$$

where $\rho_{v,sat}$ and p_{sat} are saturation vapor density and saturation pressure at T_w^*, respectively. The evaporation and thermal resistances per diffusion resistance (E/D and T/D respectively) are shown as the second and third terms in the brackets. To evaluate the significance of these terms, four cases were considered as shown in Table 5-3.

Table 5-3. Four cases to quantify E/D and T/D

Liquid	water	water	ethanol	acetone
T_w^* (K)	293	373	293	293
ρ (kg/m^3)$\times 10^2$	9.98	9.58	7.89	7.90
p_{sat} (Pa)$\times 10^3$	2.34	101	5.84	24.8
h_{fg} (J/kg)$\times 10^5$	24.5	22.6	9.27	5.39
λ (W/mK)	0.60	0.68	0.17	0.16

Fig. 5-5 shows the predicted values of E/D and T/D for k=10^{-3} m/s, as the example for the 1cm-thick diffusion layer in the atmosphere. The liquid film resistance was predicted with $\delta_e U = 1\mu$m. Since this resistance decreases as liquid film thickness decreases, it is the maximum value for the micro region. It is obvious that the thermal resistance due to heat conduction in the liquid film is significantly small compared to the diffusion resistance, even for the high-temperature case. From this result, the author can assume the overall resistance to be a constant as $R^{-1} \approx (kc_5)^{-1} + c_4^{-1}$. It should be noted that this discussion does not hold for $k \to \infty$. This situation may correspond to a vacuum condition, where there is no diffusion layer and the accommodation factor becomes large due to less molecular reflection. In this limit, evaporation is controlled by kinetic and thermal resistances and the differential equation becomes nonlinear and the local maximum of evaporation flux can be seen as shown in [15].

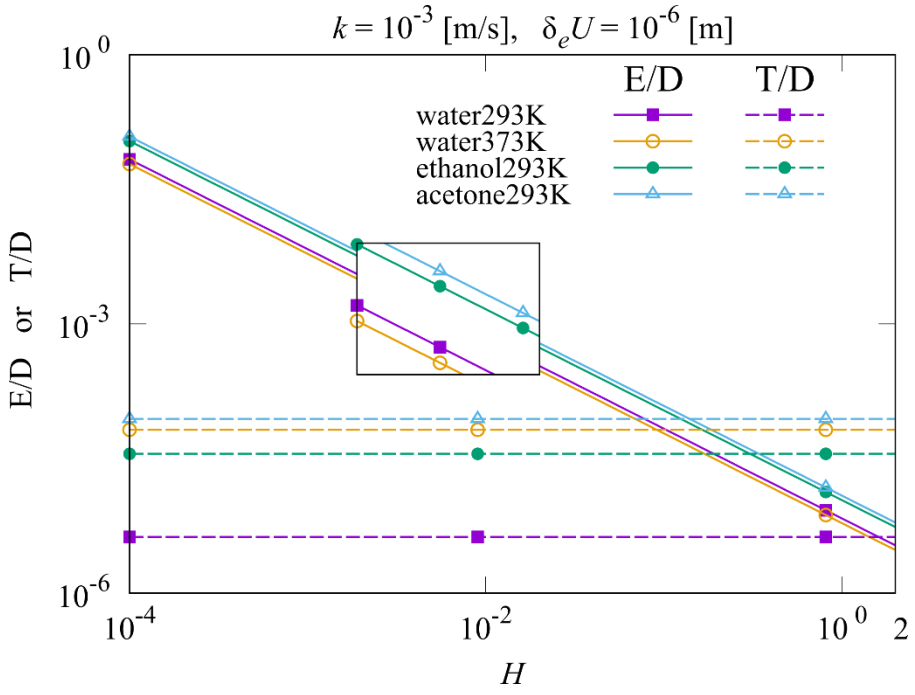

Fig. 5-5. E/D and T/D of four conditions listed in Table 5-3. Inset shows an enlarged view.

The mass flux balance equation by using Eq. (5.7) is expressed as follows;

$$\frac{d}{dX}\left(\frac{U^3}{3}\frac{dP_{ex}}{dX}\right)=R\left(\frac{P_{ex}}{\beta}-c_4^{-1}+P_{sat,T=1}-[P_v]_0\right). \tag{5.25a}$$

The Kelvin effect can be neglected for $d \gg a$. The boundary conditions of Eq. (5.25a) are

$$P_{ex} \to \beta(c_4^{-1}-P_{sat,T=1}+[P_v]_0) \quad \text{as} \quad X \to 0, \tag{5.25b}$$

$$P_{ex} \to \frac{p_d}{p'}(1-\varepsilon) \quad \text{as} \quad X \to \infty. \tag{5.25c}$$

The boundary condition of Eq. (5.25b) shows $\beta \to 0$ based on Eq. (5.9b). The second boundary condition of Eq. (5.25c) can be obtained by the boundary condition of Eq. (5.9c). Here, the equilibrium conditions are $p_d(1-\varepsilon)/p' = \beta c_4^{-1}$ and $P_{sat,T=1} = [P_v]_0$. The former condition is identical to $\varepsilon = 1$ as $\beta \to 0$.

Because the effect of thermal resistivity is significantly small as mentioned above, the solution of the above linear-O.D.E. is a monotonically increasing function with X. This result is remarkably different from that observed in the previous thermal models without the diffusion layer [15]. The sensitivity of boundary conditions at the contact line is worth mentioning. It is usually considered in numerical models where governing equations for heat and mass transfer are higher-order ODE (for example, [20]). It is known that some boundary conditions at the contact line extremely affect numerical results and therefore some techniques [63] are necessary to avoid the trivial solution (a film with constant thickness) and obtain an appropriate one. In contrast, the present model does not need any numerical scheme, hence the essential result in this model is independent on the slight change of boundary conditions (U, U' and U'') at the contact line. The maximum local evaporation flux appears at $X \to \infty$ in micro region,

$$J = R\left(\frac{p_d}{p'}\frac{1-\varepsilon}{\beta}-c_4^{-1}+P_{sat,T=1}-[P_v]_0\right) \quad \text{as} \quad X \to \infty. \tag{5.26}$$

The interfacial excess terms contribute as an excessive driving force (the first and second terms in the brackets), in addition to the conventional driving force (the third and fourth terms in the brackets). The first term exists if the system deviates from equilibrium by reducing the partial

pressure of the evaporative component and depends on a disjoining pressure. Because a disjoining pressure at the contact line is proportional to a large-scale interface curvature, the evaporation flux depends on the curvature. Only the first term in the brackets shows an enhancing effect on evaporation flux by large-scale interfacial curvatures, and it may not be negligible due to small β even for a small deviation from the equilibrium. If diffusion resistance is much greater than evaporation resistance, Eq. (5.26) can be rearranged as follows:

$$\frac{J}{R(P_{sat,T=1}-[P_v]_0)} = \hat{J} \approx \frac{1-\varepsilon}{\beta}\frac{p_d}{p_{sat}-[p_v]_0}, \tag{5.27}$$

or by using Eq. (5.9c),

$$\hat{J} = \frac{1-\varepsilon}{\varepsilon\beta}\frac{\sigma\cos\theta}{(p_{sat}-[p_v]_0)d} \quad \text{as} \quad X \to \infty. \tag{5.28}$$

Eq. (5.28) is the resulting expression for evaporation flux in this model. It must be noted that a free parameter β must be included. It is because local thermodynamic equilibrium was not assumed. The significance in Eq. (5.28) is to show evaporation may depend on a geometrical configuration of the narrow channel. Actually, it can be found that this equation is the same form as the scaling law showing the dependence of evaporation rates on interface shape, presented in Chapter 4, by rearranging Eq. (5.28) and taking j as the area-averaged evaporation flux. Fig. 5-6 shows the experimental data in Section 3.3.1 for the same wettability condition fitted with Eq. (5.28). This figure shows β is much less than $1-\varepsilon$, for example, $\beta = 7.4\times10^{-5}$ for $1-\varepsilon = 0.1$. j was set to be the area-averaged flux, where the interface areas were estimated by assuming that an interface is a cylindrical shape. The mutual diffusivity of the air-vapor system was theoretically evaluated [57]. The fitting for the hydrophilic case of the experiments mentioned in Section 2.3.2 is shown in Fig. 5-7. The tendency that a narrower channel exhibits stronger evaporation was successfully correlated. Interestingly, the good agreement was also found for the hydrophobic case as shown in Fig. 5-8 despite the model was constructed for hydrophilic conditions. It may suggest that excess pressure balances with the stress fields for hydrophobic conditions.

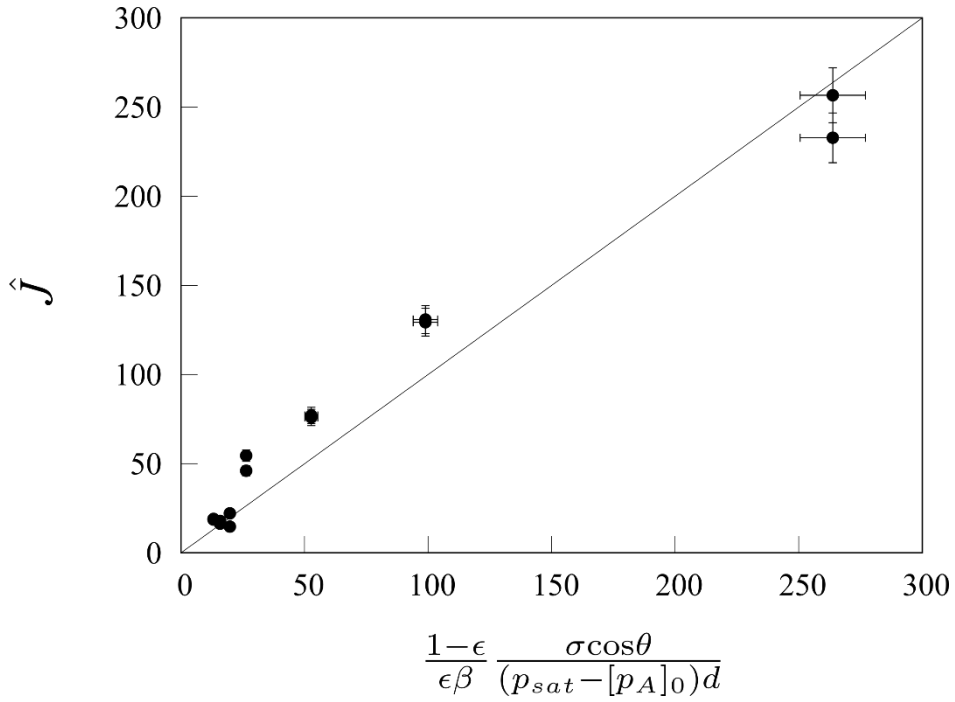

Fig. 5-6. Evaporation flux for $\theta \ll 1$: solid circle denotes experimental data in Section 3.3.1; line denotes Eq. (5.28) with a fitting parameter $1-\varepsilon/\varepsilon\beta = 1.5\times10^{3}$. Diffusion length sale was calculated by $\sqrt{4Dt}$ with $t = 600$ s and $[p_v]_0 = 0$ Pa. Error bars show the standard deviation of data (vertical axis) and of the fitting parameter (horizontal axis).

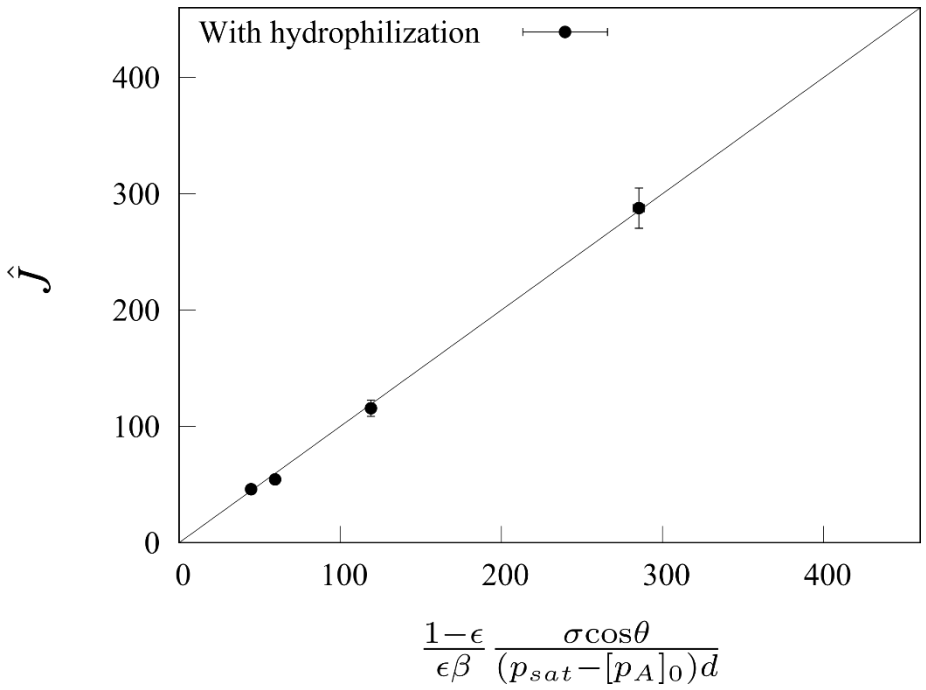

Fig. 5-7. Fitting ($1-\varepsilon/\varepsilon\beta = 2.2\times10^3$) for hydrophilic case in Section 2.3.2. Diffusion length sale was calculated by $\sqrt{4Dt}$ with $t = 600$ s, $[p_v]_0 = 0$ Pa, and $\cos\theta = (\cos\theta_{left} + \cos\theta_{right})/2$.

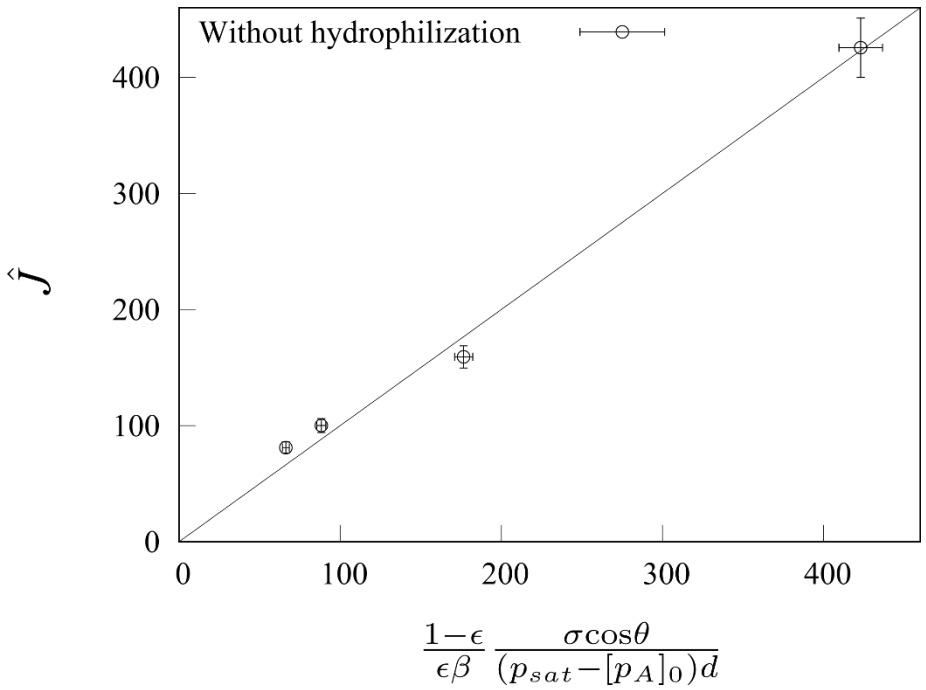

Fig. 5-8. Fitting ($1-\varepsilon/\varepsilon\beta = 7.3\times10^3$) for hydrophobic case in Section 2.3.2. Diffusion length sale was calculated by $\sqrt{4Dt}$ with $t = 600\,\mathrm{s}$ and $[p_v]_0 = 0\,\mathrm{Pa}$.

5.6 Discussions

The evaporation enhancing effect has been attributed to 2 possible physics in previous studies; one is the strong evaporation flux in the thin-film region for pure vapor condition and another is an increase in interface area due to nanoscopic precursor film for nanochannel. In the case of evaporation of macroscopic meniscus in the presence of the diffusion layer, however, the thermal resistance of the liquid film is negligibly small and the additional evaporating area due to precursor nanofilm may not be significant compared to the intrinsic meniscus [36]. Therefore, the excess vapor pressure acting as a size-dependent source term for evaporation was introduced. Conversely, the author cannot deny the possibility that the non-isothermal effect might also exist for pure vapor conditions and evaporation in a nanochannel. If so, the size-dependent evaporation flux in the hydrophobic nanopore [35] could be explained with this effect. To further investigate the evaporation enhancing effect, experiments and analysis based on non-isothermal and isothermal models would be necessary.

The present model shows the evaporation flux could depend on the interface curvature of the intrinsic meniscus. From this result, different size-dependence is extrapolated for the condition of d longer than capillary length $\kappa_{cap}^{-1} = \sqrt{\sigma/\rho g}$, because a characteristic length of the intrinsic meniscus is constant κ_{cap}^{-1} and the evaporation flux is expected to be different between the contact area and flat area. The experimental results mentioned in Section 3.3.1 shows, if $d > \kappa_{cap}^{-1}$, the apparent evaporation flux slightly depends on the ratio of contact area to total interface area, but the dependence of apparent evaporation flux on channel size is significantly reduced because of the constant curvature. The experimental results using cuvettes discussed in Section 3.3.2 also confirm the change in the size-dependence around $d = \kappa_{cap}^{-1}$. In the cuvette experiments, since each meniscus may have the same diffusion length scale in one experiment, the increase in the gradient for 5mm, 2mm and 1mm cases cannot be explained without assuming a source term depending on the channel size. Hence, the result supports the necessity of the excess vapor pressure acting as a source term for $d < \kappa_{cap}^{-1}$.

While the motivation for introducing the additional term is based on experimental results, the physical background is worth discussing. In the conventional theories, the pressure term was treated as the stress field associated with flow caused by evaporation [15]. On the other hand, the author uses it as a source term when the system deviates from the equilibrium. Considering that the equilibrium condition of Eq. (5.2) is defined by minimizing free energy, the excess pressure term can be interpreted to come from an excess quantity of free energy which arises when the

system deviates from the equilibrium. In this sense, the excess vapor pressure should be derived from its original free energy functional of Eq. (5.1), that is another way to substantiate its existence. If it is possible, there will be no necessity to introduce the difficult-to-decide parameter β. This will be also helpful to discuss the boundary condition under which non-isothermal effect should be considered, however, at this moment, the practical way may be to conduct comprehensive experiments at various boundary conditions. Next work would include comprehensive experiments at various boundary conditions (such as temperature, pressure, liquid property, wettability), which will lead to empirical correlations of the enhancing effect of capillary evaporation.

5.7 Summary

In the present chapter, a new phenomenological model is proposed for the evaporation of wetting liquid film in a narrow channel. The local heat and mass transfer in the microscopic liquid film region were described with considering heat conduction in liquid film, kinetics, and vapor diffusion. Because several basic equations in the previous models for thermodynamics and mechanical equilibrium did not hold in the investigated binary system, the minimum free energy technique was used to identify a microscopic length scale. In this model, the local thermodynamic equilibrium in micro- and macroscopic meniscus regions was not assumed, and the author introduced an excess pressure term balancing a conventional stress term at gas/liquid interface. The maximum local evaporation flux was found at the macroscopic meniscus region if the diffusion layer exists. Although a free parameter must be included because the local thermodynamic equilibrium was not assumed, the phenomenological model makes clear that a non-isothermal driving force causes stronger evaporation in a narrower channel.

Chapter 6 Conclusions

6.1 Conclusions

In the present study, the author investigated the evaporation in millimeter-scale channels to reveal how evaporation kinetics depends on the channel geometry, by means of experiments and modeling. The experimental setup was designed to parameterize the perimeter and curvature of meniscus via the channel size d by using rectangle and circular channels. The evaporation rate and flux, as well as the apparent contact angle and temperature of solid wall surface, were obtained in the presence of air. It was found that the dependence of evaporation flux on the channel size d is different whether d is larger than capillary length κ_{cap}^{-1}, or less than κ_{cap}^{-1}. The general conclusions obtained by the experiments can be summarized as follows.

Effect of curvature on evaporation flux

In the case of $d \le \kappa_{cap}^{-1}$ where the meniscus curvature is a function of the channel size, apparent and area-averaged evaporation flux was found to increase with reducing channel size and with the increase in interface curvature. This trend is consistent with previous experiments where volatile organic liquid evaporated from capillary tubes, however, the present data cannot be explained with the theory which shows evaporation flux is a function of the perimeter. The result shows the evaporation flux could strongly depend on the meniscus curvature. In the case of $d > \kappa_{cap}^{-1}$, the meniscus curvature is not a function of the channel size.

Effect of perimeter on evaporation flux

The apparent evaporation flux for $d > \kappa_{cap}^{-1}$ was found to slightly increase with the increase in the inner perimeter of the channel. This result implies strong evaporation at the contact area relative to the planer interface, and thus the apparent evaporation flux depends on the ratio of the contact area to the total interface area, although the size-dependence is not significant compared to the size-dependence due to the curvature for $d \le \kappa_{cap}^{-1}$. In the case of $d \le \kappa_{cap}^{-1}$, it was found that ten times difference in the perimeter did not affect the evaporation flux.

In the modeling works, first, the mathematical expression to show the dependence of the evaporation rate on the meniscus curvature was developed. By using the macroscopic model

considering diffusive vapor mass transport, the scaling law relating the maximum evaporation rates to the interface shape was derived and the qualitative and quantitative agreement was found with experimental data. Lastly, to explain the evaporation enhancing effect in the narrow channel, the author proposed a conjecture that there exists a certain evaporation source at the gas/liquid interface and it depends on channel size. By introducing the excess pressure term balancing the conventional stress term at gas/liquid interface into the microscopic model considering the film conduction, kinetics, and vapor diffusion, the author demonstrated that the non-isothermal driving force causes stronger evaporation in narrower channels. The experimental data showing the enhancing effect was successfully correlated by the phenomenological model and it was found that the expression for the evaporation flux in the macro region is consistent with the scaling law.

6.2 Scientific and engieering applications

The experiments and modeling works conducted in this study revealed fundamental aspects of the evaporation of wetting film. One is that the evaporation kinetics depends on the confinement structure. The result could be applied to the fabrication of functional material, reported in Nature [2]. With dip-coating and evaporation processes, they assembled chiral colloidal particles into the films functioning optical filters and into biomimetic tissue. The complex and hierarchically-organized structure results from the meniscus evaporation, whereby particle interaction in a meniscus and interfacial forces at contact-line are involved. The size-dependence of evaporation in confinements could be used to control the functionality of the film. The fact that narrower channel exhibits strong evaporation flux could be also applied to design phase-change heat exchangers, such as micro heat pipes, V-grooved heat pipes. These heat exchangers demand thermal management with high heat fluxes. The present study gives a guideline, that the conflicting parameters, the interface area and interface curvature, should be maximized with inhomogeneities of the channels (like, obstacles, channel geometry). The theoretical prediction for microscopic contact angle, in the model presented in Chapter 5, may be applied to various wetting conditions, not only completely wetting conditions. The author believes that, if so, the discussion can be expanded to the controlling wettability, which will be useful for engineering problems. The validation for the theoretical expressions using experimental or numerical data would be essential for future researches.

Reference

[1] J. Park, J. Moon, Control of colloidal particle deposit patterns within picoliter droplets ejected by ink-jet printing, Langmuir. 22 (2006) 3506–3513.

[2] W.J. Chung, J.W. Oh, K. Kwak, B.Y. Lee, J. Meyer, Biomimetic self-templating supramolecular structures, Nature. 478 (2011) 364–368.

[3] M. Khayet, Membranes and theoretical modeling of membrane distillation: A review, Adv. Colloid Interface Sci. 164 (2011) 56–88.

[4] H. Ghasemi, G. Ni, A.M. Marconnet, J. Loomis, S. Yerci, N. Miljkovic, G. Chen, Solar steam generation by heat localization, Nat. Commun. 5 (2014) 1–7.

[5] P.-G. de Gennes, F. Brochard-Wyart, D. Quéré, Capillarity and Wetting Phenomena, Springer New York, 2004.

[6] V.P. Carey, Liquid-Vapor Phase-Change Phenomena, in: S. School (Ed.), Liq. Phase-Change Phenom., 2008: pp. 253–344.

[7] B. V. Derjaguin, N. V. Churaev, Polymolecular adsorption and capillary condensation in narrow slit pores, Prog. Surf. Sci. 40 (1992) 173–191.

[8] H. Wang, S. V. Garimella, J.Y. Murthy, An analytical solution for the total heat transfer in the thin-film region of an evaporating meniscus, Int. J. Heat Mass Transf. 51 (2008) 6317–6322.

[9] S.Y. Du, Y.H. Zhao, Numerical study of conjugated heat transfer in evaporating thin-films near the contact line, Int. J. Heat Mass Transf. 55 (2012) 61–68.

[10] J. Polansky, T. Kaya, Stability of an evaporating meniscus: Part I - Theoretical analysis, Int. J. Therm. Sci. 107 (2016) 209–219.

[11] P. Stephan, J. Hammer, A new model for nucleate boiling heat transfer, Heat Mass Transf. Stoffuebertragung. 30 (1994) 119–125.

[12] P.C. Stephan, C.A. Busse, Analysis of the heat transfer coefficient of grooved heat pipe evaporator walls, Int. J. Heat Mass Transf. 35 (1992) 383–391.

[13] K. Ibrahem, M.F. Abd Rabbo, T. Gambaryan-Roisman, P. Stephan, Experimental investigation of evaporative heat transfer characteristics at the 3-phase contact line, Exp. Therm. Fluid Sci. 34 (2010) 1036–1041.

[14] M. Potash, P.C. Wayner, Evaporation from a two-dimensional extended meniscus, Int. J. Heat Mass Transf. 15 (1972) 1851–1863.

[15] S. Moosman, G.M. Homsy, Evaporating menisci of wetting fluids, J. Colloid Interface Sci. 73 (1980) 212–223.

[16] S. DasGupta, J.A. Schonberg, I.Y. Kim, P.C. Wayner, Use of the Augmented Young-Laplace Equation to Model Equilibrium and Evaporating Extended Menisci, J. Colloid

Interface Sci. 157 (1993) 332–342.

[17] S. DasGupta, J.A. Schonberg, P.C. Wayner, Investigation of an Evaporating Extended Meniscus Based on the Augmented Young–Laplace Equation, J. Heat Transfer. 115 (1993) 201.

[18] S. DasGupta, I.Y. Kim, P.C. Wayner, Use of the Kelvin-Clapeyron Equation to Model an Evaporating Curved Microfilm, J. Heat Transfer. 116 (1994) 1007–1015.

[19] S.J.S. Morris, The evaporating meniscus in a channel, J. Fluid Mech. 494 (2003) 297–317.

[20] H. Wang, S. V. Garimella, J.Y. Murthy, Characteristics of an evaporating thin film in a microchannel, Int. J. Heat Mass Transf. 50 (2007) 3933–3942.

[21] P.C. Wayner, The effect of interfacial mass transport on flow in thin liquid films, Colloids and Surfaces. 52 (1991) 71–84.

[22] P.G. De Gennes, Wetting: Statics and dynamics, Rev. Mod. Phys. 57 (1985) 827–863.

[23] P.C. Wayner, J.A. Schonberg, S. DasGupta, Effect of Interfacial Forces on Evaporative Heat Transfer in a Meniscus, 1991.

[24] S. Dasgupta, J.L. Plawsky, P.C. Wayner, Interfacial force field characterization in a constrained vapor bubble thermosyphon, AIChE J. 41 (1995) 2140–2149.

[25] F. Renk, P.C. Wayner, G.M. Homsy, On the transition between a wetting film and a capillary meniscus, J. Colloid Interface Sci. 67 (1978) 408–414.

[26] S.S. Panchamgam, J.L. Plawsky, P.C. Wayner, Spreading Characteristics and Microscale Evaporative Heat Transfer in an Ultrathin Film Containing a Binary Mixture, J. Heat Transfer. 128 (2006) 1266.

[27] S.S. Panchamgam, J.L. Plawsky, P.C. Wayner, Microscale heat transfer in an evaporating moving extended meniscus, Exp. Therm. Fluid Sci. 30 (2006) 745–754.

[28] S.S. Panchamgam, J.L. Plawsky, P.C. Wayner, Experimental Evaluation of Marangoni Shear in the Contact Line Region of an Evaporating 99+% Pure Octane Meniscus, J. Heat Transfer. 129 (2007) 1476.

[29] S.S. Panchamgam, A. Chatterjee, J.L. Plawsky, P.C. Wayner, Comprehensive experimental and theoretical study of fluid flow and heat transfer in a microscopic evaporating meniscus in a miniature heat exchanger, Int. J. Heat Mass Transf. 51 (2008) 5368–5379.

[30] C. Höhmann, P. Stephan, Microscale temperature measurement at an evaporating liquid meniscus, Exp. Therm. Fluid Sci. 26 (2002) 157–162.

[31] H.K. Dhavaleswarapu, S. V. Garimella, J.Y. Murthy, Microscale Temperature Measurements Near the Triple Line of an Evaporating Thin Liquid Film, J. Heat Transfer. 131 (2009) 61501.

[32] C.P. Migliaccio, H.K. Dhavaleswarapu, S. V. Garimella, Temperature measurements near the contact line of an evaporating meniscus V-groove, Int. J. Heat Mass Transf. 54 (2011) 1520–1526.

[33] Y. Li, M.A. Alibakhshi, Y. Zhao, C. Duan, Exploring Ultimate Water Capillary Evaporation in Nanoscale Conduits, Nano Lett. 17 (2017) 4813–4819.

[34] S. Narayanan, A.G. Fedorov, Y.K. Joshi, Interfacial transport of evaporating water confined in nanopores, Langmuir. 27 (2011) 10666–10676.

[35] Y. Li, H. Chen, S. Xiao, M.A. Alibakhshi, C.W. Lo, M.C. Lu, C. Duan, Ultrafast Diameter-Dependent Water Evaporation from Nanopores, ACS Nano. 13 (2019) 3363–3372.

[36] H. Wang, From Contact Line Structures to Wetting Dynamics, Langmuir. 35 (2019) 10233–10245.

[37] C. Buffone, K. Sefiane, IR measurements of interfacial temperature during phase change in a confined environment, Exp. Therm. Fluid Sci. 29 (2004) 65–74.

[38] C. Buffone, K. Sefiane, C. Minetti, The effect of wall thickness and material on Marangoni driven convection in capillaries, Colloids Surfaces A Physicochem. Eng. Asp. 481 (2015) 384–392.

[39] C. Buffone, K. Sefiane, J.R.E. Christy, Experimental investigation of the hydrodynamics and stability of an evaporating wetting film placed in a temperature gradient, Appl. Therm. Eng. 24 (2004) 1157–1170.

[40] C. Buffone, K. Sefiane, J.R.E. Christy, Experimental investigation of self-induced thermocapillary convection for an evaporating meniscus in capillary tubes using micro-particle image velocimetry, Phys. Fluids. 17 (2005) 1–18.

[41] C. Buffone, K. Sefiane, W. Easson, Marangoni-driven instabilities of an evaporating liquid-vapor interface, Phys. Rev. E - Stat. Nonlinear, Soft Matter Phys. 71 (2005) 3–10.

[42] C. Buffone, K. Sefiane, Investigation of thermocapillary convective patterns and their role in the enhancement of evaporation from pores, Int. J. Multiph. Flow. 30 (2004) 1071–1091.

[43] K. Sefiane, C.A. Ward, Recent advances on thermocapillary flows and interfacial conditions during the evaporation of liquids, Adv. Colloid Interface Sci. 134 (2007) 201–223.

[44] C. Buffone, K. Sefiane, J. Christy, Infra-Red measurements of an evaporating meniscus with imposed contact angle, Int. J. Therm. Sci. 121 (2017) 89–98.

[45] T.E. Daubert, R.P. Danner, Physical and thermodynamic properties of pure chemicals: data compilation, Taylor and Francis, Washington, D.C., 2013.

[46] P.G. de Gennes, F. Brochard-Wyart, D. Quéré, Gouttes, bulles, perles et ondes, Belin,

2002.

[47] S. Jung, H. Kim, An experimental method to simultaneously measure the dynamics and heat transfer associated with a single bubble during nucleate boiling on a horizontal surface, Int. J. Heat Mass Transf. 73 (2014) 365–375.

[48] S.J. Gokhale, J.L. Plawsky, P.C. Wayner, S. DasGupta, Inferred pressure gradient and fluid flow in a condensing sessile droplet based on the measured thickness profile, Phys. Fluids. 16 (2004) 1942–1955.

[49] S.J. Gokhale, J.L. Plawsky, P.C. Wayner, Experimental investigation of contact angle, curvature, and contact line motion in dropwise condensation and evaporation, J. Colloid Interface Sci. 259 (2003) 354–366.

[50] J.L. Plawsky, S.S. Panchamgam, S.J. Gokhale, P.C. Wayner, S. DasGupta, A study of the oscillating corner meniscus in a vertical constrained vapor bubble system, Superlattices Microstruct. 35 (2004) 559–572.

[51] S.S. Panchamgam, S.J. Gokhale, J.L. Plawsky, S. DasGupta, P.C. Wayner, Experimental Determination of the Effect of Disjoining Pressure on Shear in the Contact Line Region of a Moving Evaporating Thin Film, J. Heat Transfer. 127 (2005) 231–243.

[52] J.N. Israelachvili, Intermolecular and Surface Forces: Third Edition, 2011.

[53] P.J. Sáenz, A.W. Wray, Z. Che, O.K. Matar, P. Valluri, J. Kim, K. Sefiane, Dynamics and universal scaling law in geometrically-controlled sessile drop evaporation, Nat. Commun. 8 (2017) 14783.

[54] R.D. Deegan, O. Bakajin, T.F. Dupont, G. Huber, S.R. Nagel, T.A. Witten, Capillary flow as the cause of ring stains from dried liquid drops, Nature. (1997).

[55] H. Hu, R.G. Larson, Evaporation of a sessile droplet on a substrate, J. Phys. Chem. B. 106 (2002) 1334–1344.

[56] A.-M. Cazabat, G. Guéna, Evaporation of macroscopic sessile droplets, Soft Matter. 6 (2010) 2591–2612.

[57] T.K. Sherwood, R.L. Pigford, C.R. Wilke, Mass Transfer, McGraw-Hill, 1975.

[58] A.G. Osborn, D.R. Douslin, Vapor-Pressure Relations for 15 Hydrocarbons, J. Chem. Eng. Data. 19 (1974) 114–117.

[59] P.C. Wayner, Adsorption and capillary condensation at the contact line in change of phase heat transfer, Int. J. Heat Mass Transf. 25 (1982) 707–713.

[60] R.W.Schrage, A theoretical study of interphase mass transfer, Columbia University Press, New York, 1953.

[61] S. Fujikawa, T. Yano, M. Watanabe, Vapor-Liquid Interfaces, Bubbles and Droplets, Springer Science & Business Media, 2011.

[62] J.B. Young, The condensation and evaporation of liquid droplets at arbitrary Knudsen

number in the presence of an inert gas, Int. J. Heat Mass Transf. 36 (1993) 2941–2956.
[63] H. Wang, Z. Pan, Z. Chen, Thin-liquid-film evaporation at contact line, Front. Energy Power Eng. China. 3 (2009) 141–151.